SHELL ANALYSIS OF STEEL FRAMES CONSIDERING LOW-CYCLE FATIGUE WITHIN THE CONTINUUM-DAMAGE-PLASTICITY FRAMEWORK

Siamak Delir Jafarzadehazar

A Thesis

In

The Department

Of

Building, Civil and Environmental Engineering

Presented in Partial Fulfillment of the Requirements

for the Degree of Master of Applied Science (Civil Engineering) at

Concordia University

Montreal, Quebec, Canada

October 2020

CONCORDIA UNIVERSITY

School of Graduate Studies

This is to certify that the thesis prepared

By: **Siamak Delir Jafarzadehazar**

Entitled: **Shell Analysis of Steel Frames Considering Low-cycle Fatigue within the Continuum-Damage-Plasticity Framework**

and submitted in partial fulfillment of the requirements for the degree of

Master of Applied Science (Civil Engineering)

complies with the regulations of the University and meets the accepted standards with respect to originality and quality.

Signed by the final examining committee:

Dr. Anjan Bhowmick	Chair
Dr. Ayhan Ince	Examiner
Dr. Anjan Bhowmick	Examiner
Dr. R.Emre Erkmen	Thesis Supervisor
Dr. Lucia Tirca	Thesis Co-Supervisor

Approved by: _____

Dr. Ashutosh Bagchi, Chair
Department of Building, Civil and Environmental Engineering

October 2020_____

Dr. Mourad Debbabi, Interim Dean
Gina Cody School of Engineering and Computer Science

Abstract:

Shell analysis of steel frames considering low-cycle fatigue within the continuum damage plasticity framework

Siamak Delir Jafarzadehazar

In the event of an earthquake, steel-frames are subjected to cyclic loads. Within the earthquake duration, the accumulated strain in ductile members may cause micro-scale fracture of steel material due to low-cycle fatigue, which manifests itself as early yielding and stiffness degradation at macro-scale stress-strain relations. Steel moment resisting frame members are made of thin-walled cross-sections, for which local or lateral-torsional buckling failure mode is considered in design. In order to capture local buckling, material yielding and lateral-torsional buckling modes sophisticated modelling approaches need to be adopted. When shell elements are used, multi-axial material models are needed and for this purpose Continuum Damage Plasticity (CDP) framework is used to build an inelastic multi-axial stress-strain relationship. The CDP has the capability of representing both the permanent deformations due to the plastic component and the degradation of elastic moduli due to the damage component. Early yielding and stiffness degradation of the material can be captured by adopting hardening/softening and damage accumulation criteria specific to the low-cycle behaviour of metals. In this research, an in-house computer program was developed. The program has the capabilities to impose Multi-Pont Constraints (MPC) which makes it flexible to generate the meshes for columns, beams and panel zones separately and then

to bring them together. After validation of the program by using results of studies from literature, the possibilities of modelling different failure modes were investigated. MPCs were also used to simulate the beam behaviour as a special case of the shell model in which lateral-torsional buckling modes of thin-walled cross-sections of steel frames were captured under cyclic loads. It has been shown that considerations of local- and lateral-buckling modes as well as the low-cycle fatigue effect in the material cause significant differences in predicting the behaviour of steel frames under cyclic loads.

Acknowledgement

I would like to begin by expressing my greatest thanks to my supervisor Dr. Emre Erkmen. Without his endless help and support, none of this would be possible. I always have felt that he is supporting me any second of the time I was working on this thesis. I just can say I could not wish for better than this.

Special thanks to my co-supervisor Dr. Lucia Tirca about all the valuable guidance she provided and for all the time, she was there to listen and discuss.

Many thanks to Concordia University and its wonderful team of professors and employees who have made my years in university some that I will never forget.

I would also like to extend my deepest gratitude to the love of my life, Elahe, who held my hand every second of this time and supported me emotionally. My feelings would not fit in here if I wanted to express all, I just say thank you and I love you.

Mom, Dad you are my foundation. I will forever be indebted to you for your endless love and support. Your words of wisdom and love were always the ones to keep me going.

To my wonderful friends, I am finished! I know it took me a while, but I have finally made it and I could not have done it without you! I have held all your words of encouragement near and dear to my heart. Thank you!

Table of Contents

List of Figures

List of Tables

CHAPTER 1: INTRODUCTION

1.1 General View

Due to the low-cycle fatigue effects, structural elements subjected to cyclic loads may fail when large input of earthquake energy is induced in the structural system during a limited number of cycles. The strains developed in ductile structural members (fuses) accumulate at higher rates and crakes cause by low-cycle fatigue start initiated. This leads to degradation of steel material followed by stiffness degradation of structural member. To model the failure caused by fatigue is important because it can trigger the member failure. Employing the Continuum Damage Plasticity (CDP) framework to model the fatigue effect, it is an alternative method consisting in predicting the material behaviour such as a change in mechanical properties due to the different types of loading. Numerical modelling can provide good insight into understanding and predicting the structural response under fatigue effects. In the proposed method, the steel I-shape members of steel frames are modelled using shell elements.

On one hand, the shell elements used to model the thin-walled structural members might be able to capture the buckling behaviour. Deformations of cross-sections due to local buckling and distortional buckling, as well as, global deformations such as flexural, lateral and torsional buckling, can be modelled using shell elements. From the other hand, traditional beam elements are limited to rigid cross-section assumptions and therefore, cannot capture local or distortional modes. A shell element formulation can be formed by superimposing membrane and plate components, where the in-plane stretching and shear are captured by the membrane component, while bending and torsional actions are captured by plate components. The material models adopted in the shell element formulations, however, should be multi-axial and therefore,

continuum plasticity and/or damage-based material models are often adopted in shell type elements.

1.2 Objectives and Scope

The objectives of this research are:

- To develop a computer program for numerical modelling of thin-walled steel frame structures using shell elements able to perform geometric and material nonlinear analysis.
- To implement imperfections in the nonlinear analysis based on modal shapes as well as to develop a computer program for eigenvalue analysis of thin-walled steel frame structures using shell element to identify imperfections.
- To implement fatigue effects under the Continuum Damage Plasticity framework by developing a coupled elasto-plastic stress return algorithm.
- To perform nonlinear analysis using second-order geometric and material nonlinearity for monotonic load and cyclic load capturing local and global deformations considering fatigue effect.

1.3 Thesis Organization

This thesis contains six chapters:

Chapter 1 includes the introduction and objectives.

Chapter 2 contains a literature review conducted on fatigue damage. In particular, fatigue effect modelling under Continuum Damage Plasticity is reviewed. The underlying mechanisms related to damage evolution, damage modelling under the elastic-plastic damage framework and its implementation with reference to material behavior transposed into the finite element method, are

discussed. Meanwhile, the finite element methods and their evolution from a mathematical formulation to a modelling technique are presented.

The detailed overview of the need to understand the fatigue effects on the mechanical properties of the material are also presented. Afterward, the novelty of the research and its implementations are explained.

Chapter 3 describes the methodology by underlying the relationship between different mechanical characteristics of material and the formulation of fatigue damage models presented in the literature. The basic formulation related to this research regarding material modelling and fatigue implementation into the Continuum Damage Plasticity framework is also presented. The finite element method formulation used in this study is explained, as well as, its capabilities in the modelling of frame structures of thin-walled sections are discussed. The developed formulation also uses Multi-point Constraint for assemblage purposes, as well as, to introduce kinematic constraints.

Chapter 4 presents the algorithmic details and characteristics of the numerical model developed for finite element analysis purposes and the material constants adopted in the model presented in Chapter 3.

Chapter 5 contains the frame analysis results. The modal analysis deformation graphs for different types of modelling are presented. Then, the frame response subjected to monotonic load and cyclic load is included. A comparison is conducted to show the difference in response between the case when fatigue damage is considered and not considered.

Chapter 6 concludes the research and provides guidelines for future work.

CHAPTER 2. LITERATURE REVIEW

2.1 Fatigue damage

Mechanical failure in metals is an important phenomenon and extensive research have been conducted since 19th century (Krupp 2007). It has been observed that metals (mostly shafts in the steam machine) have specific life when they are subjected to cyclic loading. After the railroad tragedy (1500 casualties) that involved a train heading to Paris in 1842, research work on metal failure has been increased and the term “fatigue” was introduced by Braithwaite in 1854 (Smith 1842, Braithwaite 1854). Experiments related to the fatigue behaviour of the axle of the railroad were firstly conducted by Wöhler (1870) who tried to find the mechanism for systematic fatigue-life prediction. He used a 5000-km reference route to measure the strain and found out that at the time of passing over switches, there are high peaks of strain recorded. The study led scientists to relate the number of cycles in loading to the maximum allowable stress. These studies have led to the Wöhler diagram (Also named as S-N Curve Diagram). Prof. Johann Bauschinger from the Technical University of Munich, found a reduction in plastic yield stress after returning from plastic tension to plastic compression and vice versa (Krupp 2007).

After advances made on microscopic observation, in 1903, Ewing and Humfrey (1903) conducted microscopic observation of microstructural mechanism during the cyclic deformation of metals. They found that a specimen subjected to bending could experience growth in slip bands in certain crystallites that lead to developing fatigue crack (Ewing et al. 1903). Palmgreen and Miner conducted additional experiments on the variation of stress amplitude during fatigue life and supported the hypothesis of linear damage accumulation and proposed the following equation (Palmgreen 1924, Miner 1945).

$$\sum_i \frac{N_i}{N_{fi}} = 1.0 \tag{2.1}$$

In Eq.2.1, also known as Miner Rule, the N_i is the number of cycles at a specific stress amplitude, and N_{fi} is the number of cycles that the material fails due to the same stress amplitude.

Base on the observations of fracture in material due to inhomogeneity, the field of fracture mechanics has been formed and the failure prediction can be made based on the local stress concentrations and energy parameters (Inglis 1913, Griffith 1920). The fracture related to notches that have an influence on reduction in fatigue life, was another theory which lead to the introduction of fatigue notch factors by August Thum (Technical University of Darmstadt) and Heinz Neuber (Technical University of Munich) (Neuber 1961).

The development in dislocation theory introduced by Polanyi (1934) and Orowan (1939) was a step forward in the research addressing metal fatigue. This research was further used by Hirsch (1956), who used electron microscopy to observe dislocation in metal structure. The improvement in testing machines and theory was leading scientists to develop formulas that relate different mechanical properties to fatigue damage. Later on, Manson (1953) and Coffin (1954) proposed to relate the number of cycles to plastic strain. After Tempsom et al. (1956) presented the importance of persistent slip bands, Zappfe and Worden (1955) and Forsyth and Ryder (1960) conducted research on the phenomenon of the occurrence of striations of fractured surface in metal samples subjected to fatigue. At the same time, Irwin (1958) used the term “stress-intensity factor” K in static fracture analysis, which is presented in Eq.2.2. Then, a relationship between change in stress-intensity factor and defect grow rate as showed in Eq. 2.3 was proposed (Neuber, 1961) and the equation was named as Paris’ Law (Krupp 2007).

$$K = \sigma\sqrt{\pi a}Y \tag{2.2}$$

$$\frac{\mathrm{d}a}{\mathrm{d}N} = C\Delta K^n \tag{2.3}$$

where K is the stress intensity factor, a is the crack length, σ is the mechanical stress, Y is geometry function, C and n are material-specific constants.

Modifications were made on the Paris' Law by Elber (1968, 1971), who noticed that fatigue-related fracture could be developed before complete unloading, even after simple tensile load. Finally, Shiozawa (1996) and Tokaji (2003) introduced fatigue initiation and propagation in material microstructures that can lead to fatigue failure (Krupp 2007).

Along with the later studies on fatigue damage using experiments and microscopic observations, numerical techniques were developed to model the damage that occurs in the material. This damage can be related to material mechanical properties, loading protocol, etc.

As a general view, the damage is a defect caused by any disorder in material such as missing bonds connecting molecules or any miss connecting in microstructure such as microvoids. However, this disorder cannot be measured by any non-destructive test made in situ and in general, the measurements have to be done by modelling the effect of this disorder in the behavior of the material. By using loading and unloading of the material, the load deflection curve can be divided into four major groups shown in Fig. 2.1.

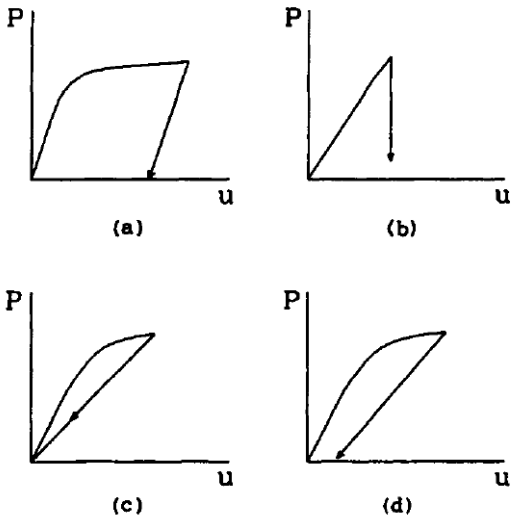

Fig. 2.1 Load deflection curves: (a) ductile, (b) perfectly brittle, (c) quasi-brittle, (d) ductile-brittle response (Krajcinovic 1996)

The ductile material (Fig. 2.1 a) becomes plastic after an elastic deformation, and it follows the elastic pattern at the point of unloading. The brittle is defined as the material that is not ductile. The perfectly brittle material (Fig. 2.1 b) does not show any plastic behaviour and fails at the time that damage occurs.

Early studies of McClintock (1968) showed that microvoids are the basic mechanism of the failure process. Within the framework of damage mechanics, Krajcinovic (1996) categorized the models in three major groups: statistic models, micromechanical models and continuum models. These models can be applied to different types of materials such as steel and concrete; also, each of these models had been applied to different cases that made them popular among scientists. Paul (2014) presented a study based on multi-axial low-cycle fatigue life prediction. In the study, the main idea was to provide a model to predict fatigue life for constant amplitude multi-axial proportional and non-proportional loadings and compare the results with experimental studies.

To simulate the observed multi-axial stress-strain relationships in materials often coupled plasticity and damage formulations are needed. The plasticity component captures the evolution of permanent deformations whereas the damage component captures the stiffness degradation in the behaviour. Inglessis et al. (1999) proposed a yield function of damage for a plastic hinge with the evolution of damage and kinematic hardening using a model that took into account the damage softening and degradation in the stiffness for both monotonic and cyclic load patterns and had an acceptable verification of experimental and numerical. Around the same time, Armero et al. (2000) proposed a general framework for continuum damage mechanics coupled with plasticity, which can be used, generally, in different materials. In this framework, the general formulation is built for infinitesimal models defined considering separate surfaces of yield and damage in the stress space.

Numerical formulations adopting coupled damage and plasticity material models in structural analysis, were proposed by Ibrahimbegovic et al. (2008) based on previous work conducted by the first author (1994a and 1994b). Ayhan et al. (2013) proposed a phenomenological constitutive model of coupled damage-plasticity. They showed that the coupled plasticity model can capture the behaviour of metals including hysteresis, progressive stress relaxation to zero and strain ratcheting. They have also illustrated the numerical advantages of being able to calibrate the plasticity and damage components separately by using operator splits.

Brunig and Gerke (2011) considered anisotropy in their ductile damage model. Roth and Mohr (2014) investigated the effect of strain rate on ductile fracture initiation. In their study, three sets of tensile experiments were carried out with low, intermediate, and high strain rate on a three set of specimens with flat smooth, notched, and central hole. A plasticity model with a Johnson-Cook type of rate and temperature-independency (Johnson and Cook 1985) and a combined Swift-Vose

strain hardening law (Vose 1948, Swift 1952) was used along with a non-associated anisotropic flow rule. They have shown the improved precision in capturing local strains and deformations.

Plasticity and Damage based phenomenological material models have also been used in predicting the fatigue behaviour in metals. Murakami et al. (2016) studied the loss of ductility due to low-cycle fatigue damage. They have related the effect of small cracks that are present in the material with the loss of ductility and limited life due to fatigue. Their experiments showed the correlation of crack length present in the surface and the fatigue life. They also showed that by removing surface cracks, ductility and fatigue life could be extended. Zhan et al (2016) used Continuum Damage Mechanics-based approach to predict the fatigue life of aluminum alloy. In their study, Lemaitre's plasticity damage model (1994) was used to evaluate the damage accumulation and accordingly, the fatigue life of aluminum alloy that has undergone foreign object impact. The life and the site of crack initiation were in accordance with the test results. Riberio et al. (2016) used the Finite Element Method for damage model calibration and its application on steel members. In the study, a damage failure criterion based on Continuum Damage Mechanics is used to simulate the damage evolution in the Finite Element model. The main investigation was conducted on fracture strain dependency to the triaxle stress state using numerical modelling. Lua et al. (2016) used finite element analysis for crack branching and its impact in damage prediction of aluminum structures.

Bosco and Tirca (2017) used fibre-based damage accumulation modelling to simulate the damage evolution in I-shaped steel beams. The model is based on Miner's Law to predict fatigue damage due to cyclic loading and had good agreement with related experiment results. It is worth to mention that the OpenSees fatigue model was calibrated on results from experimental tests conducted on I-shape steel beams. Aboutalebi et al. (2018) determined the damage parameters and

fracture locus of the St12 steel using numerical and experimental results. The main goal of the study was to determine ductile damage parameters using a convenient tensile test and to avoid difficult complex tests. Springer and Pettermann (2018) developed a multi-axial damage model to predict fatigue life under low-cycle loading. The model is based on continuum damage mechanics accumulating based on the plastic work done, and for numerical modelling, a solid based element is used. A study of real-time cycle counting, and energy-based critical plane criterion based on multi-axial fatigue damage evaluation was presented by Xue et al. (2019). In their study, all the stress and strain components were considered and then, the damage evaluation method for multi-axial random loading is used along with proposed online cycle counting. Modelling of welded joints of steel shell structures was performed by Radu et al. (2020). The fatigue damage modelling used is based on Paris' Law, and for numerical modelling, solid elements are used. An assessment of fatigue damage is also proposed in the design phase to be considered.

2.2 Shell Element

Ahmad et al. (1970) used curved finite elements for analyzing thick and thin shell structures. In the study, the curved and arbitrary shape of the elements used for modelling is introduced along with axisymmetric situations. This type of element was useful in modelling curved structures such as tanks, pipes, etc. and makes it more convenient to analysis; otherwise, a very fine mesh is required to model the curved parts to reduce the model error. Hughes and Liu (1981) performed a quasi-static nonlinear analysis of shell element, which accounts for large strain and rotation effects using a three-dimensional finite element. Several numerical modelling examples are also provided in the study. In the second part of this study, Hughes and Li (1981), provided a simplified implementation of a three-dimensional shell as a two-dimensional shell. The introduced shell element can be used to model tubes, beams, columns and assemble of these elements.

Batoz and Tahar (1982) presented a quadrilateral element for thin plate bending modelling named as Discrete Kirchhoff Quadrilateral. In the element, based on Discrete Kirchhoff Technique, the 3 degrees of freedom was used for each of four nodes and the results of the convergence were satisfactory compared to other plate element modelling types.

Jetteur and Frey (1986) described a nonlinear shallow thin shell element with a curved quadrilateral with four nodes in the corner and six degrees of freedom in each node. The element consisted of membrane and plate element, and the curvature was dealt with Marguerre's theory. It was indicated in the study that it should be given more attention to the element locking.

Fafard et al. (1987) presented the Discrete Kirchhoff method as a general two-dimensional thin plate/shell theory assembling of flat elements. Using the proposed method, in a three-dimensional space, the in-plane buckling modes can be captured. In the model, they used assumptions leading to the formulation of thin-walled structures and then assessed the numerical examples provided considering different constraints. Lateral-torsional buckling can also be captured.

Gruttmann et al. (1992) introduced a shell element coupling of membrane element with drilling degree of freedom and plate element with Reissner-Mindlin type kinematic assumption. In the study, it was concluded that the resulting Euler-Lagrangian equations preserve equilibrium, the symmetry of the stress resultants, and the equality of independent and displacement independent rotation field.

Cook (1994) used a basic formulation for modelling shell-type element by writing the membrane and bending stiffness matrices for a flat geometry and adding them. For this purpose, a 24 degree of freedom quadrilateral shell element formulation is presented, providing the proposed element functionality in different cases, although comparing results show good performance against the

former studies. Ibrahimbegovic (1994a, 1994b) introduced the formulation for a geometrically nonlinear shell with drilling rotation around shell normal in the description of finite shell rotations. The finite deformation theory of a three-dimensional continuum with an independent rotation field was identified in the study. In the second part of the study (1994b), the application of a geometrically nonlinear shell with drilling rotation around shell normal was presented. The consistency of the tangent stiffness matrix is also investigated regarding different convergence rates presented. It was shown in the results that the element is capable of capturing local deformations.

Chapelle and Bathe (1998) presented fundamental considerations for the finite element analysis of shell structures regarding the thickness and related formulations. They concluded that considering small thickness, the shell element behavior consisting of membrane and plate showed small change in shell behavior.

Classical shell theories were examined as a numerical method by Teng and Hong (1998). In the study, the numerical and buckling analysis was presented as a set of nonlinear strain-displacement problems. The analytical and numerical comparison made on some shell theories with a special case of Rotter and Jumikis theory, and as a result, some comments were provided for various shell theories for use in numerical buckling analysis of complex branched shells.

Areias et al. (2005) provided an improvement to the 16 degrees-of-freedom quadrilateral shell element using Kirchhoff-Love constraints. In the study, an immune to locking or unstable nodes formulation as a combination of constitutive continuum law with classical shell kinematics is presented. Compared to the other elements in former studies, the element proposed has a good performance in both linear and nonlinear cases and the mesh distortion sensitivity is low. The element formulation is made without any significant assumptions.

Nguyen-Van et al. (2009) presented a flat quadrilateral element for shell structural analysis. The element is the result of the coupling membrane with drilling degree of freedom and bending elements for analyzing arbitrary shell structures. The provided element is a four-node element with 6 degrees of freedom for each node. In the membrane part, the provided formulation is developed by incorporating a strain smoothing technique. This technique helps the membrane to avoid shear locking due to the drilling degree of freedom. The performance of this element was better than other uniform shell elements.

2.3 Imperfections

Calladine (1995) presented an investigation on understanding imperfection sensitivity in the buckling of thin-walled shells. In the study, various buckling modes, nonlinear behavior, geometric imperfection under load, etc. were introduced. The idea of "locked-in" initial stresses is considered if imperfect initial geometry and also static indeterminacy of boundary conditions claimed to have an effect on the buckling load.

The study of implementing random geometrical imperfection in the buckling analysis of I-shaped steel frames was provided by Papadopoulos et al. (2013). The material and geometrical nonlinear finite element analysis is performed to capture the buckling behavior in frames introducing a number of random imperfect geometries simulated with detailed discretization in shell element.

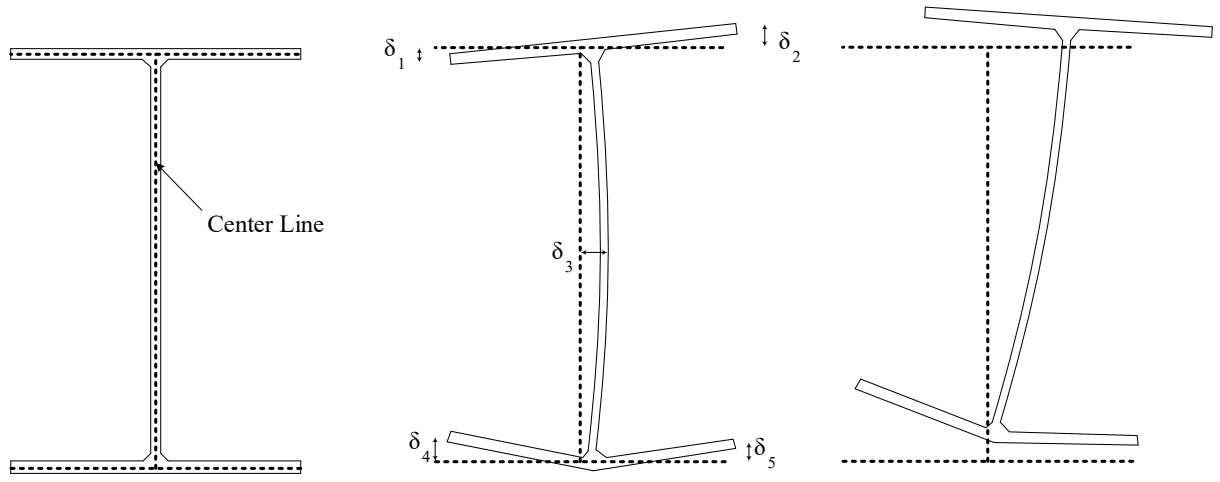

Fig.2.2 Buckling as the geometrical imperfection a) perfect b) local imperfection c) global and local imperfection (Papadopoulos et al. 2013)

Shayan et al. (2014) introduced the modelling of initial geometric imperfections of steel frames insisting on the influence of shape and magnitude of the imperfection on the behavior. Using eigenmodes obtained from elastic buckling analysis was also proposed in the study. Furthermore, investigations regarding the number of modes and magnitude of the mode combinations were performed in the study.

Hutchinson and Thompson (2018) provided some examples of highly sensitive shell structures such as cylindrical structure subjected to axial compression and built a relationship between the buckling load and the shape of imperfection in the model. For this purpose, the elastic buckling analysis is performed. Luo et al. (2019) performed a buckling assessment of thin-walled structures considering geometrical imperfection. In the study, the uncertainty of such geometrical imperfections was modelled by a non-probabilistic field model. As an imperfection, the thickness of the shell was chosen, and different buckling shapes were captured using finite element analysis.

CHAPTER 3. CONSIDERING FATIGUE DAMAGE WITHIN ELASTO PLASTIC DAMAGE FRAMEWORK

It was discussed in the literature review that fatigue failure in metals is one of the common failure mechanisms in both structural and mechanical components. In this study, a coupled plasticity-damage model was used to consider fatigue effects within shell element analysis of steel frames. The motivation for this study is to capture the local, as well as, the global deformations considering the changes in the material behaviour due to fatigue damage under cyclic loading.

On the other hand, shell type finite element is widely used for the analysis of thin-walled structures. The method has been studied and improved over the decades. Several references from the literature have introduced and discussed the use of shell elements. As examples can be mentioned the followings: the finite element analysis of plates and tanks (Cheung et al. 1965), axisymmetric composite structures (Rashid 1966), convergence in FEM (Tong and Pian 1967), elastic membranes (Oden 1967), finite element for plate bending (de Veubeke 1968) and the finite element of flexible shells (Wempner 1969). Implementation of a material model within shell elements require phenomenological frameworks such as plasticity and/or damage.

3.1 Elastic Plastic Damage Framework

In this chapter, the primary formulation for the Continuum Damage Plasticity framework and its formulation is provided. In this framework, the damage of the modelled material due to different causes affect its properties and will lead to different behavior of the material due to loads. The term damage is flagged with *d* as well as *e* for elastic and *p* for plastic. Three major groups are provided to introduce this framework (Armero and Oller 2000):

1- Total strain includes elastic, plastic, and damage part:

$$\varepsilon = \varepsilon^e + \varepsilon^p + \varepsilon^d \tag{3.1}$$

To illustrate this formula, ε^e is the strain that will be recovered after unloading, ε^p is the strain that cannot be retrieved after unloading, and ε^d is the reversible strain associated with damage due to change in elasticity modulus. To make it clear, damage related strain is coupled with plastic strain, and it evolves due to plastic behavior, while it causes evolution in elasticity modulus. In Fig.3.1, the stress strain relationship including the plastic strain, elastic strain, and damage strain, are shown.

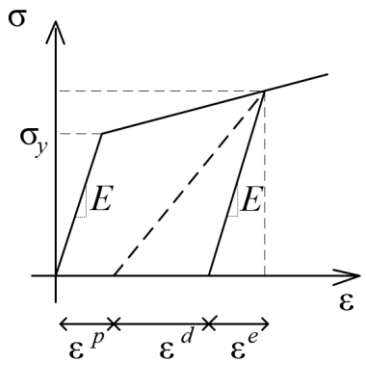

Fig.3.1. Strain decomposition in the 1D case.

2- Total strain energy due to plasticity and damage

$$\psi(\varepsilon, \varepsilon^d, D, \xi^d, \varepsilon^p, \xi^p, \kappa^p) = \psi^e(\varepsilon^e) + \psi^d(\varepsilon^d, D) + \Xi^p(\xi^p) + \Xi^d(\xi^d) + \Lambda^p(\kappa^p) \tag{3.2}$$

where $\Xi^p(\xi^p)$, $\Lambda^p(\kappa^p)$ and $\Xi^d(\xi^d)$ are functions for hardening proposed by Ibrahimbegovic et al. (2008).

3- The yield criteria and the damage associated with it can be introduced as:

$$\phi^p(\sigma, q^p, \alpha) \le 0; \phi^d(\sigma, q^d) \le 0 \tag{3.3}$$

where the terms q^p, α, and q^p are related to hardening and damage conjugate to ξ^p , κ^p and ξ^d

The latter can be defined as:

$$q^p = -\frac{\partial \Xi^p}{\partial \xi^p} = -K\xi^p \tag{3.4}$$

$$\alpha = \frac{\partial \Lambda^p}{\partial \kappa^p} = -H\kappa^p \tag{3.5}$$

$$q^d = -\frac{\partial \Xi^d}{\partial \xi^d} = -K^d\xi^d \tag{3.6}$$

where K^p, K^d, and H are related to hardening values from initial values of the plastic behavior, and σ_y is the yield stress.

These three conditions will be explained in detail in the following sub-sections.

3.1.1 **Strain decomposition**

As mentioned before, the total strain can be defined as three different parts, which are: elastic, plastic, and damage strain (Armero and Oller, 2000). In the uniaxial case, this decomposition is presented in Fig.3.2.

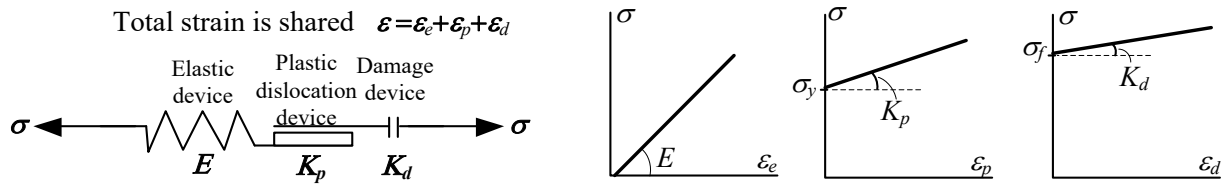

Fig.3.2. Strain decomposition (Erkmen, 2019)

As shown in Fig.3.2, the elastic, plastic, and damage components of the strain are connected in series where E, K^p, K^d, σ_y, and σ_f are the elastic modulus, plastic hardening modulus, damage

hardening modulus, yield stress limit, and the fracture initiation stress limit, respectively. While the plastic part provides irreversible strain, the other two parts, elastic and damage, provide reversible strains. In this framework, the plastic and damage parts are separate and they have their own strain values. However, the plastic and damage parts are connected is series, which means that it should be provided an equilibrium between the damage and plasticity. In the process of computing, the stresses based on plasticity and damage will be updated to match using the iterative procedure. Lately illustrated, by using some constraints, the plasticity and damage will be coupled.

3.1.2 Total strain energy

The main objective of using the total strain energy is to separate the damaged and undamaged parts of the strain. To derive the stress at the given point, the elastic strain multiplied with elasticity modulus will provide the stress. In this derivation, there are two assumptions required: (1) elastic deformations are small compared with the plastic deformations, (2) there is an elastic strain function based on Cauchy stress $\bar{\sigma}$ and elastic strain $\psi^e(\varepsilon^e)$. The elastic strain energy can be defined as:

$$\psi^e(\varepsilon^e) = \frac{1}{2}\varepsilon^e : C^e : \varepsilon^e \tag{3.7}$$

As the material is undamaged, the relationship between stress and strain is presented in the equation below. In this part, it is accepted that the damage is coupled with plasticity and undamaged have the same power of no plastic behavior. The term E refers to elasticity modulus as a scaler value, and C refers to the second-order elasticity modulus tensor.

$$\bar{\sigma} = E\varepsilon^e \tag{3.8}$$

Using the Legendre transformation, the elastic strain energy can be introduced as provided in the following equations (Ibrahimbegovic et al., 2008):

$$\psi^e(\varepsilon^e) = \sigma : \varepsilon^e - \chi^e(\sigma); \qquad (3.9)$$
$$\chi^e(\sigma) = \frac{1}{2}\bar{\sigma} : C^e : \bar{\sigma}$$

The same definition can be derived for the strain energy related to damage.

$$\psi^d(\varepsilon^d, D) = \sigma : \varepsilon^d - \chi^d(\sigma, D); \qquad (3.10)$$
$$\chi^d(\sigma, D) = \frac{1}{2}\sigma : D : \sigma$$

3.1.3 Plasticity

3.1.3.1 Yield criteria

The schematic yield mechanism for a 1D (1-Dimension) case was presented in Fig.3.2. To further illustrate the yield condition and material behavior in the 1D case, the mild steel tensile loading can be taken into account. The normal stress - strain diagram for mild steel (ductile material) is provided in Fig.3.3.

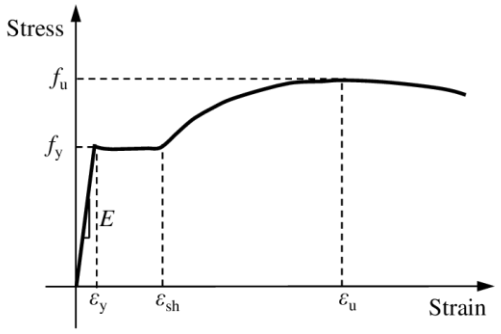

Fig.3.3. Normal stress- strain of a ductile material 1D case

As mentioned before, the inelastic part is complete recovery after unloading the specimen. As long as the material is in the elastic range, the material behaves as elastic, the stress is proportional to the strain, and the Hook's law is applicable. After going into the plastic part, some parts of the strain can be recovered after unloading, and there will be some residual strain after complete unloading. In the plastic part, Hook's Law is not applicable because the stress and strain are not proportional anymore. After the plastic plateau part, the material tries to resist any additional loading, and it means that strain increase. There should be additional loading on the specimen, which is known as hardening. The afterward behavior is known as necking and there will be some strain headed to fracture without adding external load. Fig.3.4 is provided to compare the idealized behavior of the material in the presence of hardening.

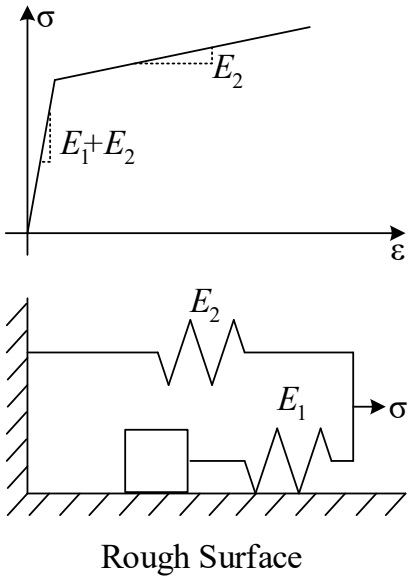

Fig.3.4 Linear hardening behavior (Erkmen, 2019)

Herein, the elastic modulus of material is decomposed as E1 and E2. After a specified threshold, the spring E_1 cannot deform and the mass starts to move. This move represents the unrecoverable strain.

In 3D cases, the yield condition is a bit different from the 1D case. The elastic limit of the material is defined by the specified yield criterion under combined stresses, but of course, it is related to 1D yield stress. The 3D yield condition is related to material properties and state of stress, where there are different hypotheses about the condition of the yielding. The yielding condition can generally be expressed as the following formula:

$$f_y(\sigma_{ij}, \alpha, \beta, ...) \tag{3.11}$$

where σ is the present state of stress and α, β, etc. are material properties defining the yield condition. A well known theory about yielding condition is provided by Von Misses, which can be expressed as follows:

$$\sigma_{eff} = \sigma_y \tag{3.12}$$

$$\sigma_{eff} = \sqrt{\frac{1}{2}\left(\left(\sigma_{xx} - \sigma_{yy}\right)^2 + \left(\sigma_{yy} - \sigma_{zz}\right)^2 + \left(\sigma_{xx} - \sigma_{zz}\right)^2 + 6\left(\tau_{xy} + \tau_{zy} + \tau_{xz}\right)^2\right)} \tag{3.13}$$

It can be understood from these formulas that if the combined state of stress, named as effective stress, reaches the yield limit, then, the yielding starts. In Fig. 3.5-a it is presented the yield surface in principle stress space, and in Fig.3.5-b, the yield criteria in the deviatoric plane (Chen et al. 1988).

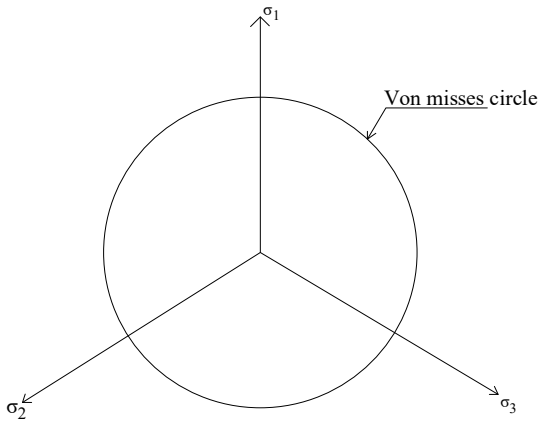

Fig.3.5a The yield surface in principle stress space (Chen et al. 1988)

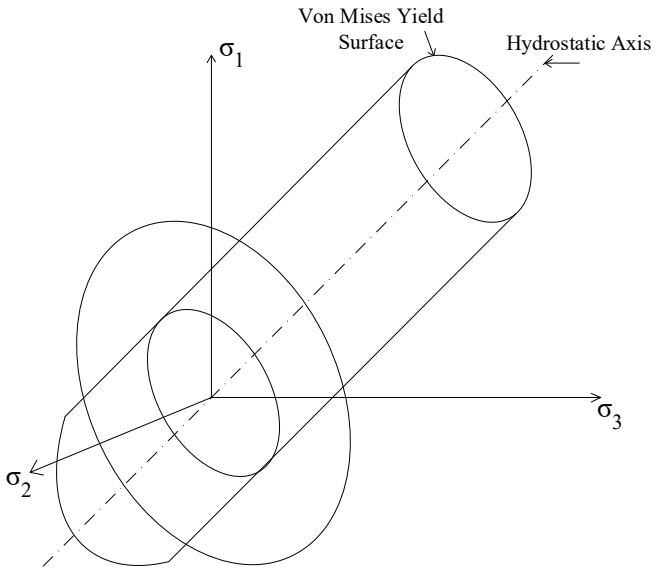

Fig.3.5b. The yield criteria in the deviatoric plane (Chen et al. 1988)

Considering Elastic perfect-plastic behavior, the stress is proportional to the elastic strain.

$$\mathrm{d}\sigma = E\mathrm{d}\varepsilon^{e} \tag{3.14}$$

The yield condition that should always be satisfied by stresses for elastic perfect-plastic material can be expressed as:

$$f(\sigma) = |\sigma| - \sigma_y \leq 0 \tag{3.15}$$

The expression above indicates that if the magnitude of the stress is less than the yield stress, the material will behave elastic, and if it reaches the yield stress, it will behave as perfect plastic. In this case, there is no hardening after yielding. If the strain hardening is taken into account, there should be a parameter that affects the yielding surface named as hardening parameter. In the Fig.3.6, the stress-strain diagram of the elastoplastic behavior considering strain hardening is presented.

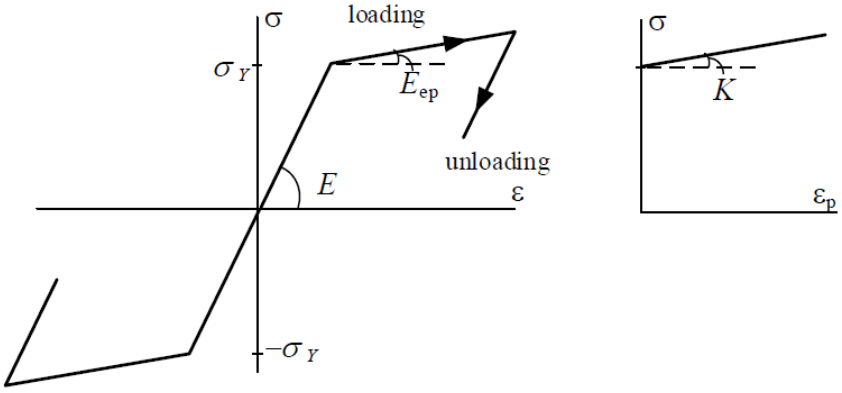

Fig.3.6 Elastoplastic material behavior with strain hardening (Erkmen, 2019)

As formerly mentioned, both K and E_{ep} are functions of κ which is named as hardening parameter. Three types of hardening are described as below as a simple overview of types of hardening in material under uniaxial loading and unloading are provided:

1. Isotropic hardening:

This type of hardening takes into account the change in yield stress value and carries from the tension zone to compression and vice versa. It is the mainly used type of hardening in numerical models. Fig.3.7a shows the isotropic hardening in the biaxial stress field.

2. Kinematic hardening:

Due to this type of hardening, the elasticity range is assumed to remain unchanged, but there is a slope in the plastic range in the stress-strain relationship. Fig.3.7b shows the kinematic hardening in the biaxial stress field.

3. Combined hardening

This type of hardening is a combination of isotropic and kinematic hardening and capable of capturing both types of material behavior.

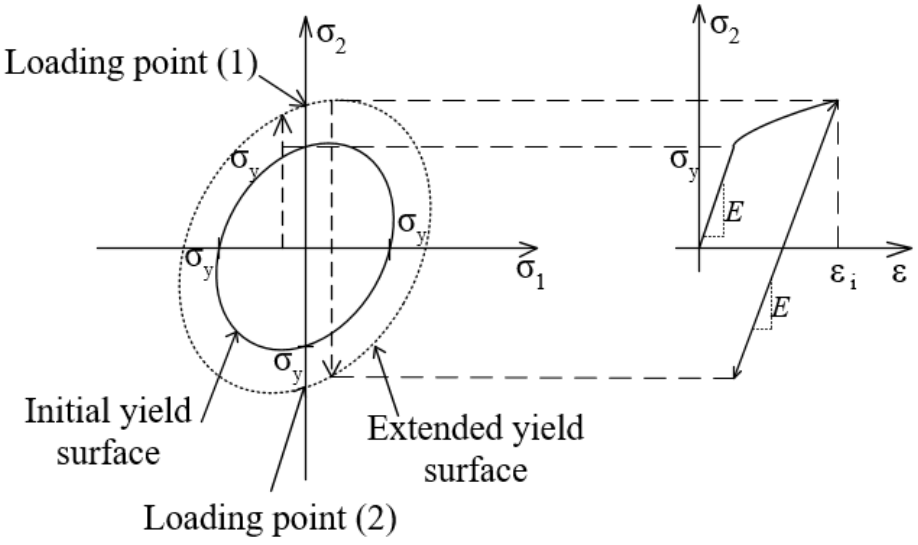

Fig.3.7a The isotropic hardening in biaxial stress field (Teymouri et al. 2019)

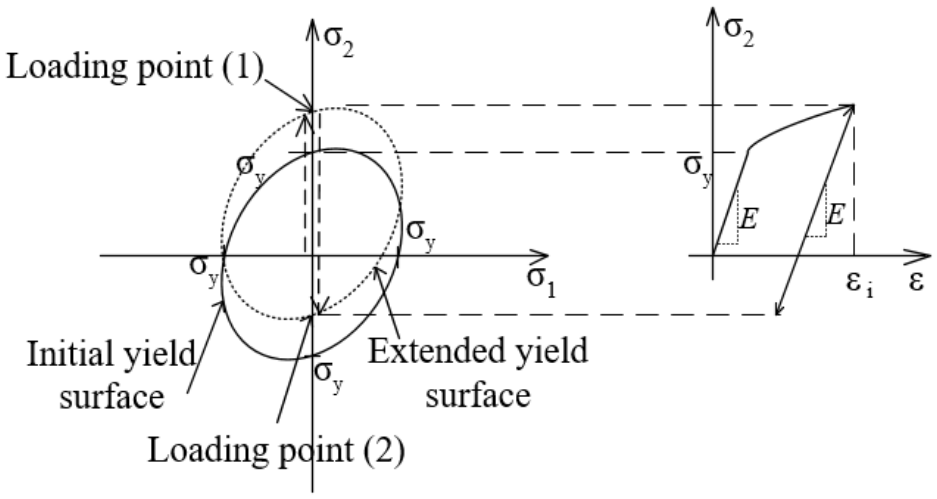

Fig.3.7b The kinematic hardening in biaxial stress field (Teymouri et al. 2019)

The aforementioned conditions excepting the yield criteria are valid and the yielding will have another parameter and can be expressed as below:

$$f(\sigma,\alpha) = |\sigma| - \left(\sigma_y + \alpha K\right) \leq 0 \tag{3.16}$$

where α is the material parameter, and K is called the elastic modulus. For K = 0, the elastic perfect-plastic material can be obtained and by K < 0, the softening (necking) can be captured.

3.1.3.1 Associated flow rule

It can be understood from the formula in Eq. (3.16) that the stress cannot pass the yielding limit so, the function $f(\sigma, \alpha) \leq 0$. The following formula can be used to determine the direction and amplitude of the plastic strain:

$$\mathrm{d}\varepsilon^p = \mathrm{d}\lambda \frac{\partial f}{\partial \sigma} \tag{3.17}$$

where the term $\mathrm{d}\lambda$ is the amplitude of the plastic strain, also named as proportionality factor, and the term $\partial f/\partial\sigma$ is the direction of the plastic strain. The presented formula is called the flow rule. If

there is no plastic deformation, then $f(\sigma, \alpha) < 0$, and if there is plastic deformation, $f(\sigma, \alpha) = 0$. Thus, according to flow rule, consistency conditions for the elastoplastic deformation can be expressed as:

$$\mathrm{d}\lambda \mathrm{d}f = 0 \tag{3.18}$$

To conclude, if $\mathrm{d}\lambda = 0$ there is no plastic deformation and $\mathrm{d}f < 0$; if $\mathrm{d}\lambda > 0$ there is plastic deformation and $\mathrm{d}f = 0$. Therefore, the stress conditions cannot address any point out of the yield surface shown in Fig.3.6, and when there exists any plastic deformation, it can move on the yield surface. It means that the stress is either inside the yield surface or on the yield surface. Considering the yield surface itself, the strain can grow larger (strain hardening) or become smaller (strain softening).

3.1.3 Damage

The definition of damage in this context is a change of load carrying area that will lead to a change in the mechanical properties of the material. To describe the damage effect, a 3D element is shown as a representative volume element in a body. Consider a damaged state that some parts of the cross-section area cannot carry any loads. The Fig.3.8 represents the mentioned state. The element surface is $\mathrm{d}A$, and if $\mathrm{d}A^d$ were considered as the damaged part of the surface, then the effective area will be (Lemaitre 1992):

$$\mathrm{d}\tilde{A} = \mathrm{d}A - \mathrm{d}A^d \tag{3.19}$$

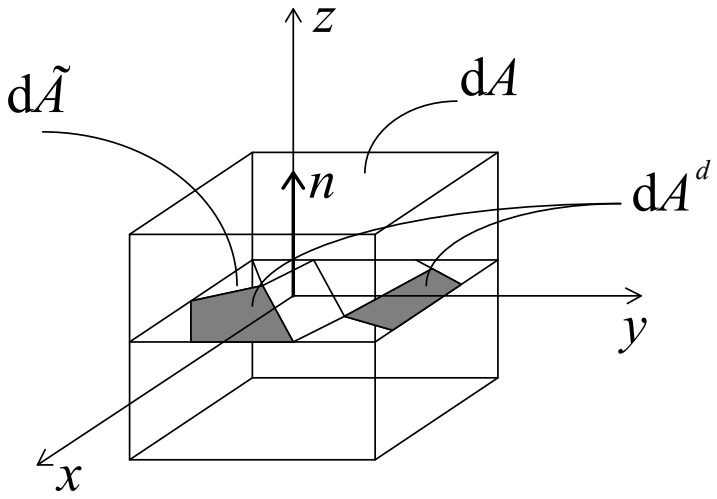

Fig.3.8 Damaged and undamaged area (Murakami 2012)

The damage variable φ and its relationship with damage parameter D can be expressed as:

$$\varphi(x,n)=\frac{\mathrm{d}\tilde{A}}{\mathrm{d}A} \tag{3.20}$$

$$D(x,n)=1-\varphi=\frac{\mathrm{d}A-\mathrm{d}\tilde{A}}{\mathrm{d}A}=\frac{\mathrm{d}A^{d}}{\mathrm{d}A} \tag{3.21}$$

It can be understood from the above relationship that for the undamaged state, $D = 0$, and for totally fractured (or failed) state, $D = 1$. By reduction in the area, the stress will be increased. Magnified stress can be expressed as:

$$\tilde{\sigma}=\frac{\mathrm{d}F}{\mathrm{d}\tilde{A}}=\frac{\sigma}{1-D} \tag{3.22}$$

The initiation of damage and reduction in the area will also cause a reduction in stiffness of the material. So, the damage state can also be expressed as a variation in elasticity modulus (Chaboche

1977). Considering a single bar capable of having damage, the following expressions can be drawn:

$$\tilde{\sigma} = E_0 \varepsilon \tag{3.23}$$

$$\sigma = E(D)\varepsilon \tag{3.24}$$

where E_0 is the elasticity modulus of the undamaged material, and *E(D)* is the elasticity modulus of damaged material (Murakami 2012). The magnified stress state can also be proportional to undamaged stress using the elasticity modulus:

$$\tilde{\sigma} = \frac{E_0}{E(D)}\sigma \tag{3.25}$$

From the above formulas, the following expressions can be obtained:

$$E(D) = (1 - D)E_0 \tag{3.26}$$

$$D = 1 - \frac{E(D)}{E_0} \tag{3.27}$$

To illustrate the deformation of elastic-plastic damaged material, consider a uniaxial tension stress-strain diagram presented in Fig.3.9a, and Fig.3.9b. It is shown that the damage starts at the point where the plastic strain reaches the threshold and then the damage increases by the increase in plastic strain. The threshold is called damage initiation plastic strain. The plastic strain fracture limit is when the damage parameter is $D = 1$.

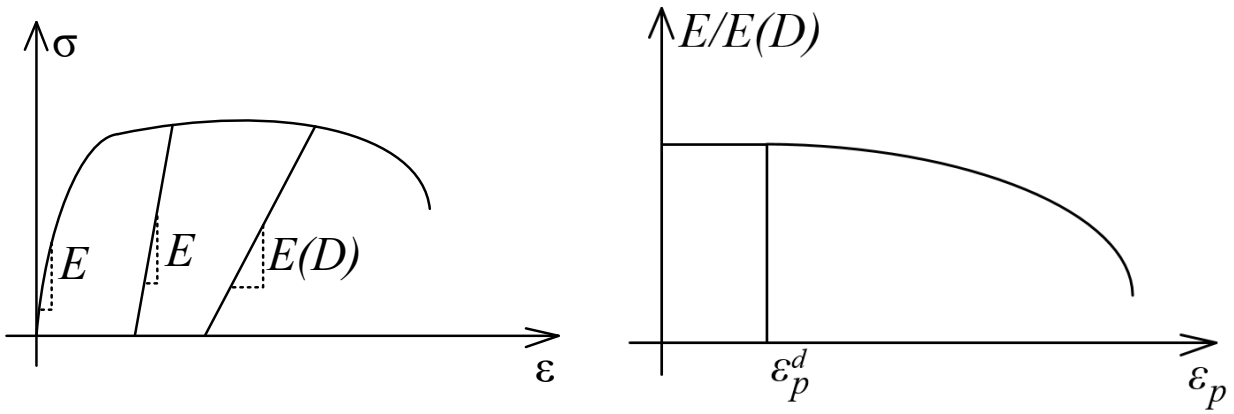

a) Stress-strain relationship b) damage vs. plastic strain

Fig.3.9 Damaged elasticity modulus a) compared to undamaged elasticity modulus, b) normalized and compared to plastic strain (Murakami 2012)

The plastic strain threshold for some materials is $\varepsilon_p^d = 0$, which means that by the time that the material is plastic, the damage starts.

3.2. Fatigue Effect

3.2.1. Fatigue regime

Failure due to fatigue can be divided into low-cycle and high-cycle regimes. In cyclic loads, the plastic deformations can separate these two regimes. In the low-cycle fatigue, the plastic deformation is considered as macroscopic and in the high-cycle fatigue the plastic deformation is considered as microscopic. This means that the plastic deformations are larger in low-cycle fatigue and can lead to failure under lower number of cycles. The number of cycles to failure in low-cycle fatigue is below 10^4 while this number for high-cycle fatigue is above 10^4. Macroscopic strain can be measured using strain gauges or other measuring instruments (Farahmand et al. 1997).

3.2.2 Fatigue effect formulation

Material subjected to cyclic load can fail in an earlier stage than under monotonic loading. This kind of failure is named as fatigue failure. Commencement and enlargement of the micro-cracks due to multiple plastic deformations are considered as the source of this kind of failure. It is accepted that the fatigue crack in metals occurs in two stages, crack initiation and crack propagation (Brown 1973). By accepting that the damage occurs with plastic deformation, damage evolution in one cycle, based on inelastic strain energy, can be expressed as provided in the following Eq. (Ellyin et al. 1984):

$$\Delta w = \int_{1cycle} \sigma . \varepsilon^{p} \mathrm{d}\varepsilon^{p} \tag{3.28}$$

After modification made on the above expression, the inelastic strain energy can be presented as (Amiable et al. 2006):

$$\Delta w_{m} = \Delta w + \alpha \sigma_{h}^{\max} \tag{3.29}$$

where α is a material parameter and $\sigma_{h}^{\max}$ is maximum hydrostatic pressure that occurs during a cycle. By combining the formulas, the following expression can be presented (Springer et al. 2018):

$$\frac{\mathrm{d}D}{\mathrm{d}N} = \frac{x_1}{l}\left(\Delta w_{m}\right)^{x_2} \tag{3.30}$$

Herein x_1 and x_2 are material properties, and l is the characteristic length obtained from element size. It results dD as the damage increment and dN the cycle increment. By integration of the formula, the damage parameter can be expressed as:

$$D = \int \frac{x_1}{l} \left(\Delta w_m \right)^{x_2} \mathrm{d}N \tag{3.31}$$

The elasticity modulus will change due to the result of Eq. (3.31) using Eq. (3.16).

3.2.2 Softening due to fatigue

The effect of cyclic load can be expressed in hardening parameter beside change in stiffness. As stated before, the stress after yielding is mostly dependent on the hardening parameter (Fig.3.7), and the hardening is dependent on material properties. After the crack initiation occurred, the energy dissipated during fracture at the end of the process, which is a cycle in this context, can be expressed as (Martinez et al. 2015):

$$W_f = \int_{V_f} g_v \mathrm{d}V \tag{3.32}$$

where g_v is the fracture energy by unit volume. It is noted that after the fracture initiated in the material, the softening happens. The function that describes the evolution of an equivalent uniaxial stress state is presented in Fig.3.10 (Martinez et al. 2015).

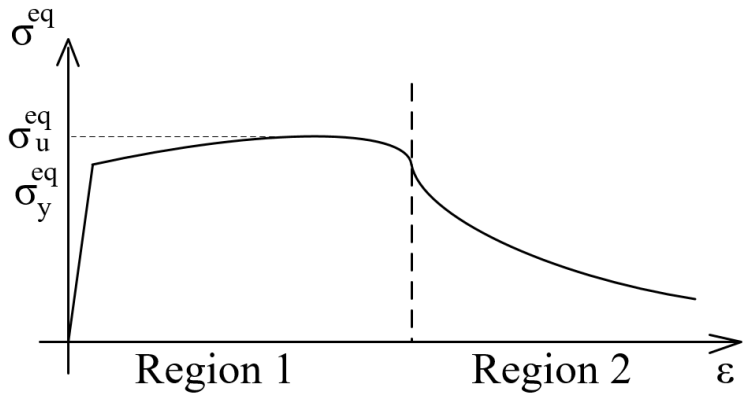

Fig.3.10 Evolution of equivalent stress (Martinez et al. 2015)

The first region is presented formerly in this chapter, and it shows the stress-strain relationship for elastic-plastic material with the effect of hardening, and the second region is defined by an exponential function to simulate softening. By the increase in plastic strain, the graph shows a relative increase in negative slope, but it is softened by an increase in strain. By this assumption, the hardening parameter, which is a scaler variable, can be defined as (Martinez et al. 2015):

$$\kappa^p = \frac{1}{g_v}\int_{t=0}^{t} \sigma : \dot{\varepsilon}^p \mathrm{d}t \tag{3.33}$$

where κ^p is the internal hardening parameter.

3.3 Algorithmic Details

3.3.1 Plasticity

The closest-point projection algorithm is adopted for the plastic return procedure. As the first step, the residual stress vector at local iteration *I,* r^{pi}, can be calculated as:

$$r^{p\,i} = \sigma^{p\,i} - (\sigma_n + E\Delta\varepsilon_n - \Delta\lambda^i\, Ea^i) \tag{3.34}$$

where σ_n is the last converged stress at the end of the previous global step, and $\sigma^{p\,i}$ is initially $\sigma_n + E\Delta\varepsilon_n$ which is updated at each local iteration *i*. It should be noted that $\Delta\lambda^i$ is initially zero, as the trial step is based on no plastic deformation assumption. The residual stress in Eq. (3.34) is then used to calculate the increment in the proportionality factor as:

$$\delta\lambda^i = \frac{f^i - a^{Ti} R^{p\,i} E^{-1} r^{p\,i}}{a^{Ti} R^{p\,i} a^i + K_p^i} \tag{3.35}$$

In Eq. (3.35), $R^{p\,i}$ is defined as:

$$R^{p\,i} = (E^{-1}Q^{p\,i})^{-1} \tag{3.36}$$

in which:

$$Q^{p\,i} = I + \Delta\lambda^i EH_b^i \tag{3.37}$$

And

$$H_b^i = \frac{\partial a^i}{\partial \sigma} \tag{3.38}$$

The f^i is evaluated by using the last updated stress $\sigma^{p\,i}$ from Eq. (3.35). The proportionality factor of plastic deformations can be then updated using:

$$\Delta\lambda^{i+1} = \Delta\lambda^i + \delta\lambda^i \tag{3.39}$$

Increment in the stress vector can be calculated as:

$$\delta\sigma^{p\,i} = -R^{p\,i}(E^{-1}r^{p\,i} + \delta\lambda^i a^i) \tag{3.40}$$

From Eq. (3.40), the stress vector can be updated as:

$$\sigma^{p\,i+1} = \sigma^{p\,i} + \delta\sigma^{p\,i} \tag{3.41}$$

3.3.2 Fatigue damage

The fatigue damage due to cyclic load is calculated after a complete cycle, and then the material is updated. As mentioned earlier in this Chapter, the cumulative plastic strain increment multiplied by the corresponding stress will be the work done due to plasticity in the cycle.

$$W = \int \mathrm{d}w = \int \sigma \mathrm{d}\varepsilon^p \tag{3.42}$$

After each cycle of loading completed, the modified work, and then the fatigue damage due to cyclic load can be expressed as below:

$$W_m = W + \alpha\sigma_{hyd} \tag{3.43}$$

$$\sigma_{hyd} = \frac{(\sigma_1 + \sigma_2 + 0)}{3} \tag{3.44}$$

$$D_{c+1} = D_c + \frac{x_1}{l}(W_m)^{x_2} \tag{3.45}$$

Then, the damage calculated affects the elasticity modulus as (Springer 2018):

$$E(D) = (1 - D)E \tag{3.46}$$

3.3.3 Hardening

Presented in previous sections, the strain hardening (and strain softening) can cause a change in yielding surface. The function used for hardening is presented below:

$$K = K_0 + H_s\sqrt{1 - \left(\frac{\xi - \xi_t + 1}{(1 + \xi_t)^2}\right)} \quad if \quad \xi < \xi_t \tag{3.47}$$

$$K = K_0 + H_s + H_{ss}\sqrt{\left(\frac{\xi - \xi_t}{(1 + \xi_t)^2}\right)}.a_f \quad if \quad \xi \geq \xi_t \tag{3.48}$$

where K_0, H_s, and H_{ss}, are material related hardening parameters and ξ_t is the plastic work related parameter which separates the hardening and softening stage of material. The parameter ξ can be expressed as below:

$$\xi = \sum dw = \sum \int \sigma\varepsilon^p \tag{3.49}$$

In Fig 3.11. the graphic that represents the formula above is presented.

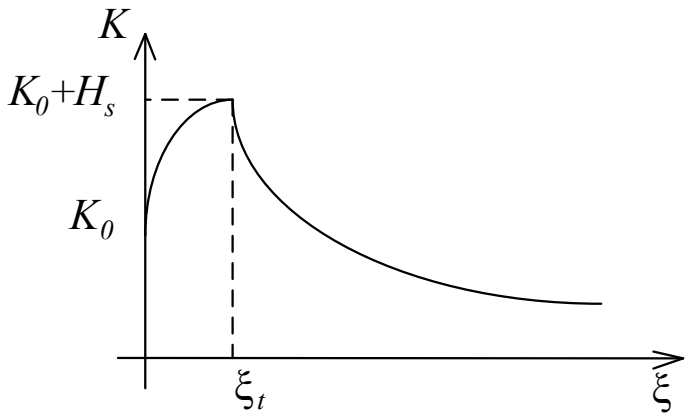

Fig.3.11 Hardening (softening)

In the procedure, hardening perform separated from the stress converging process and becomes effective after converged stress. The update process for hardening after convergence in step *i* can be expressed as:

$$\alpha_i^j = \alpha_i + \Delta\lambda_i^j + \delta\lambda... \tag{3.50}$$

The flowchart for the steps used in this study is presented below:

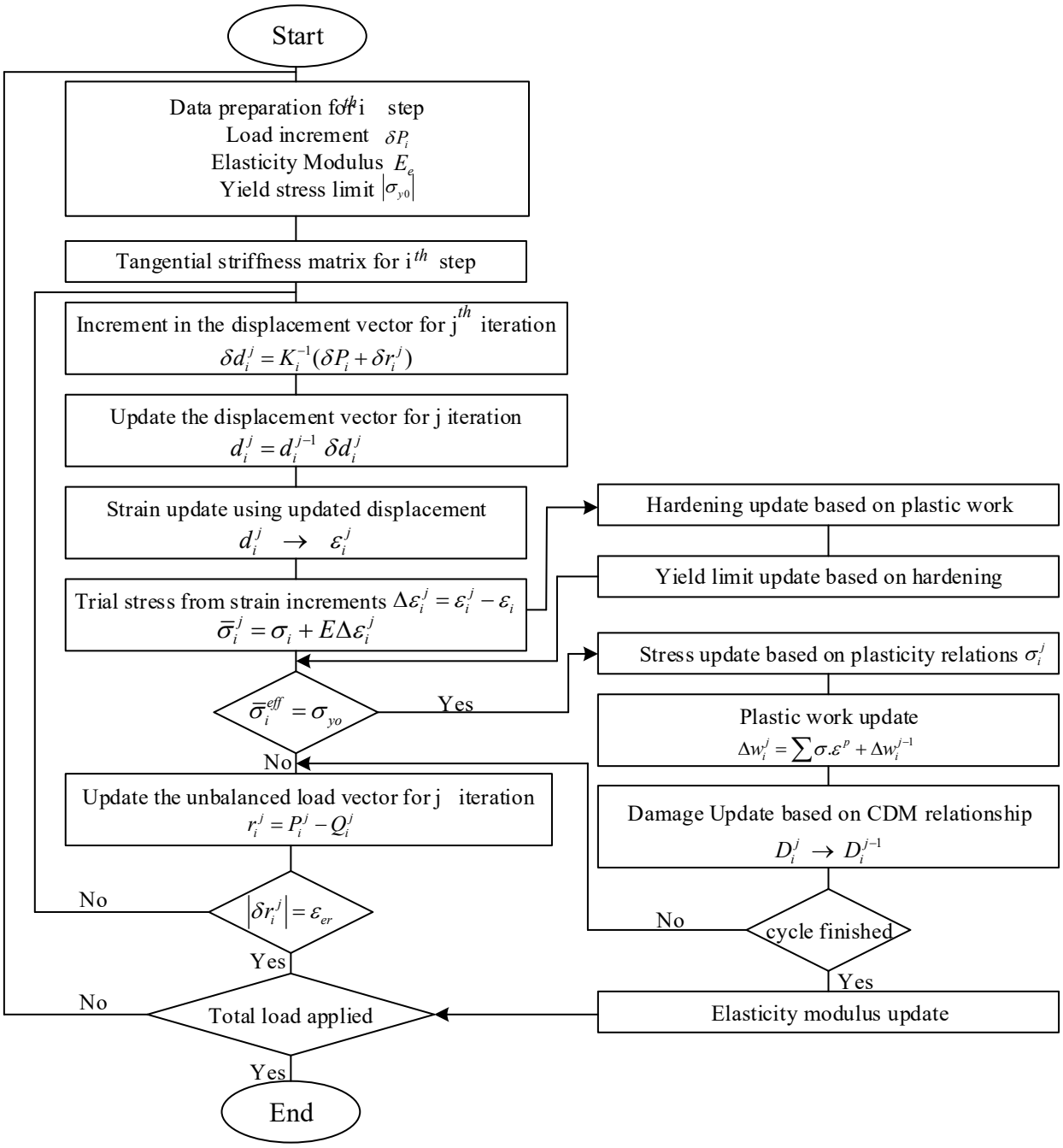

Fig.3.12 Flowchart developed and used in this study

3.4 Thin-walled Structural Modelling with Shell Elements

To model the behavior of thin-walled structures, the shell-type finite elements are used. Shell element models can capture both lateral-torsional and local buckling behavior. The shell element

is formulated as a combination of membrane-type and plate-type elements. Both membrane and plate components have four nodes so that they can be super-imposed easily. The final shell element formulation has six degrees of freedom per node, which makes it suitable for 3D analysis of structures, as shells of different orientations can be connected (e.g., web and flanges) as shown in Fig.3.13.

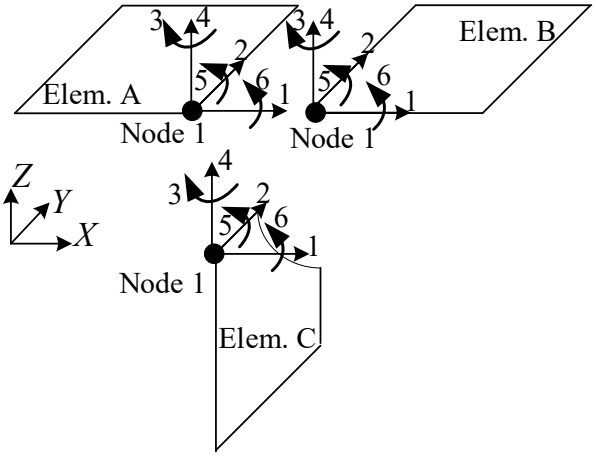

Fig.3.13 Connection of three elements at the common node (Erkmen, 2019)

The plate element is based on the Kirchhoff plate theory that neglects shear deformation effects due to bending around the neutral surface (Fig. 3.14). The four-node Discrete Kirchhoff Quadrilateral proposed by Batoz et al. (1982) was employed. The element has 3DOF per node. This element is commonly used for the analysis of thin-walled members (e.g., Farfard et al. 1987). For the four-node membrane element, the drilling degrees of freedom are introduced as described in Ibrahimbegovic et al. (1990) so that the membrane part also has 3DOF per node.

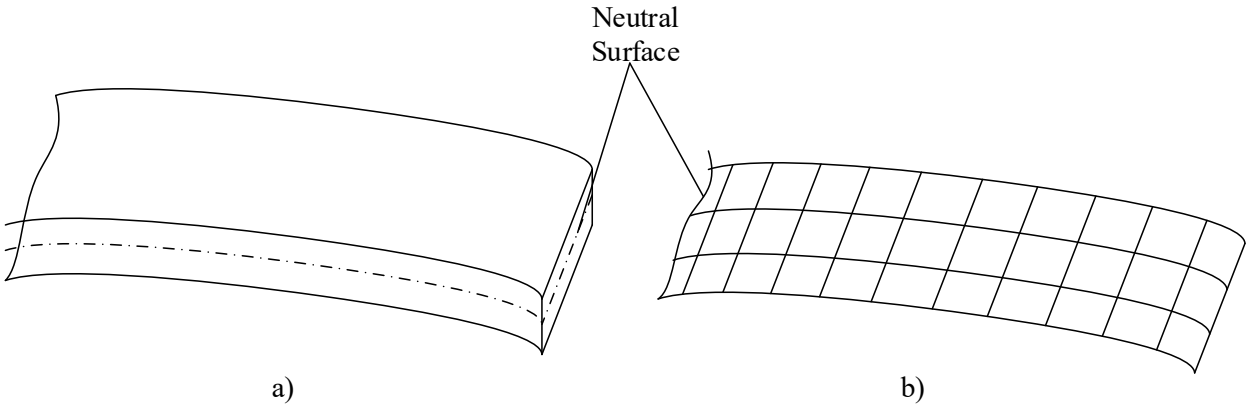

Fig.3.14 Modeling: a) thin-walled structure b) representing shell element mesh (Liu et al. 2014)

To express the shell-type element strains, deflections in *x* and *y* direction named as $\hat{u}_0$ and $\hat{v}_0$ respectively in the mid-surface of local *x–y* plane, and the out of plane deflection $\hat{w}_0$ in the local z-direction are considered. For rotations also, the bending rotations $\hat{\theta}_x$ and $\hat{\theta}_y$ in local *x–z* and *y–z* planes, drilling rotation $\hat{\theta}_z$ around z-direction can be expressed.

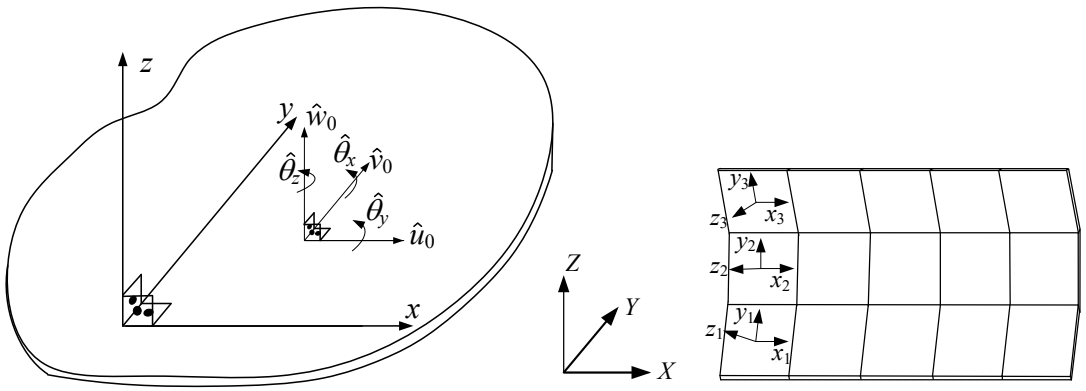

a) Local deflections of the shell element (b) Global vs. local coordinate system

Fig.3.15: Deflections and coordinate systems for the shell element formulation (Erkmen 2013)

To decompose the strain in shell element, it can be divided into two parts, which are strains due to plate bending deformation $\hat{\boldsymbol{\varepsilon}}_b$, membrane deformations $\hat{\boldsymbol{\varepsilon}}_m$ and, second-order membrane and plate bending action $\hat{\boldsymbol{\varepsilon}}_N$ presented below:

$$\boldsymbol{\varepsilon} = \hat{\boldsymbol{\varepsilon}}_b + \hat{\boldsymbol{\varepsilon}}_m + \hat{\boldsymbol{\varepsilon}}_N \tag{3.51}$$

where the plate bending strains can be written as showed below and $\hat{\boldsymbol{\chi}}$ can be defined as curvature.

$$\hat{\boldsymbol{\varepsilon}}_b = -z\begin{Bmatrix} \dfrac{\partial \hat{\theta}_x}{\partial x} \\ \dfrac{\partial \hat{\theta}_y}{\partial y} \\ \dfrac{\partial \hat{\theta}_x}{\partial y} + \dfrac{\partial \hat{\theta}_y}{\partial x} \end{Bmatrix} = -z\hat{\boldsymbol{\chi}} \tag{3.52}$$

The membrane part can be written as:

$$\hat{\boldsymbol{\varepsilon}}_m = \begin{Bmatrix} \dfrac{\partial \hat{u}_0}{\partial x} \\ \dfrac{\partial \hat{v}_0}{\partial y} \\ \dfrac{\partial \hat{u}_0}{\partial y} + \dfrac{\partial \hat{v}_0}{\partial x} \end{Bmatrix} \tag{3.53}$$

The third part mentioned above can be expressed as:

$$\hat{\boldsymbol{\varepsilon}}_N = \begin{Bmatrix} \dfrac{1}{2}\left(\dfrac{\partial \hat{w}_0}{\partial x}\right)^2 + \dfrac{1}{2}\left(\dfrac{\partial \hat{v}_0}{\partial x}\right)^2 \\ \dfrac{1}{2}\left(\dfrac{\partial \hat{w}_0}{\partial y}\right)^2 + \dfrac{1}{2}\left(\dfrac{\partial \hat{u}_0}{\partial y}\right)^2 \\ \dfrac{\partial \hat{w}_0}{\partial x}\dfrac{\partial \hat{w}_0}{\partial y} \end{Bmatrix} \tag{3.54}$$

3.4.1 Shell element formulations

3.4.1.1 Membrane component interpolation functions of shell element

The displacement vector presented in Fig.3.15 can be written as:

$$\hat{u} = \left\langle \hat{u}_0 \quad \hat{v}_0 \quad \hat{\theta}_z \quad \hat{w}_0 \quad \hat{\theta}_x \quad \hat{\theta}_y \right\rangle^T \tag{3.55}$$

which can be formed as an interpolation by deformations as:

$$\hat{\mathbf{u}} = \hat{\mathbf{X}}\hat{\mathbf{d}} \tag{3.56}$$

And element nodal displacement vector can be written as:

$$\hat{\mathrm{d}} = \left\langle \hat{u}_1 \quad \hat{v}_1 \quad \hat{\theta}_{z1} \quad \hat{w}_1 \quad \hat{\theta}_{x1} \quad \hat{\theta}_{y1} \quad \hat{u}_2 \quad \ldots \quad \hat{u}_4 \quad \hat{v}_4 \quad \hat{\theta}_{z4} \quad \hat{w}_4 \quad \hat{\theta}_{x4} \quad \hat{\theta}_{y4} \right\rangle^{\mathrm{T}} \tag{3.57}$$

And the matrix $\hat{\mathbf{X}}$ can be written as:

$$\hat{\mathbf{X}} = \left[\begin{array}{cccccc:c:c:c} N_1 & 0 & N_1^x & 0 & 0 & 0 & N_2 \ldots N_2^x \ldots & N_3 \ldots N_3^x \ldots & N_4 \ldots N_4^x \ldots \\ 0 & N_1 & N_1^y & 0 & 0 & 0 & \ldots N_2 \;\; N_2^y \ldots & \ldots N_3 \;\; N_3^y \ldots & \ldots N_4 \;\; N_4^y \ldots \\ 0 & 0 & N_1 & 0 & 0 & 0 & \ldots N_2 \ldots & \ldots N_3 \ldots & \ldots N_4 \ldots \\ 0 & 0 & 0 & N_1 & 0 & 0 & \ldots . N_2 \ldots & \ldots . N_3 \ldots & \ldots . N_4 \ldots \\ 0 & 0 & 0 & H_1^x & H_2^x & H_3^x & \ldots H_4^x \;\; H_5^x \;\; H_6^x & \ldots H_7^x \;\; H_8^x \;\; H_9^x & \ldots H_{10}^x \;\; H_{11}^x \;\; H_{12}^x \\ 0 & 0 & 0 & H_1^y & H_2^y & H_3^y & \ldots H_4^y \;\; H_5^y \;\; H_6^y & \ldots H_7^y \;\; H_8^y \;\; H_9^y & \ldots H_{10}^y \;\; H_{11}^y \;\; H_{12}^y \end{array}\right] \tag{3.58}$$

Also, terms N_i are standard bilinear shape functions which can be defined as:

$$N_i = \frac{1}{4}\left(1+\xi_i\xi\right)\left(1+\eta_i\eta\right), \; i = 1,2,3,4 \tag{3.59}$$

In the function above $\xi = x/a$ and $\eta = y/b$, and *a* and *b* are half-length of the rectangular element member in *x* and *y* directions, respectively. The coordinate system is placed in the middle of the element; therefore, $-1 \le \xi \le 1$ and $-1 \le \eta \le 1$. For the numerical integration, 2x2 and 3x3 Gaussian

quadrature was used for membrane and plate parts. In Fig.3.16, the 2x2 and 3x3 Gaussian quadrature points are presented:

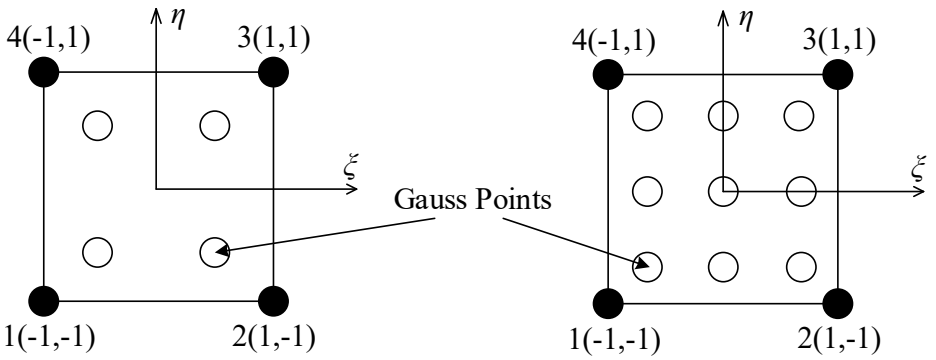

Fig.3.16 the Gaussian quadrature points a) 2x2 and b) 3x3 (Erkmen, 2019)

According to Allman-type interpolation function for membrane N_i^x and N_i^y can be defined as:

$$N_i^x = \frac{1}{8}\left(y_{ij}N_l - y_{ik}N_m\right),\ (i=1,2,3,4) \tag{3.60}$$

$$N_i^y = \frac{1}{8}\left(x_{ij}N_l - x_{ik}N_m\right),\ (i=1,2,3,4) \tag{3.61}$$

in which

$$N_m = \frac{1}{2}\left(1-\xi^2\right)\left(1+\eta_m\eta\right),\ (m=8,5,6,7) \tag{3.62}$$

$$N_l = \frac{1}{2}\left(1+\xi_l\xi\right)\left(1-\eta^2\right),\ (l=5,6,7,8) \tag{3.63}$$

where $x_{ij}=x_j-x_i$, $y_{ij}=y_j-y_i$, $l_{ij}^{\ 2}=x_{ij}^{\ 2}+y_{ij}^{\ 2}$, $(ij=41,12,23,34)$ and $(ik=12,23,34,41)$.

3.4.1.2 Plate component interpolation functions of shell element

Shape functions of the Discrete Kirchhoff Quadrilateral can be explicitly written as:

$$
\begin{aligned}
H_1^x &= 1.5\left(a_5 N_5 - a_8 N_8\right) & H_1^y &= 1.5\left(d_5 N_5 - d_8 N_8\right) \\
H_2^x &= -N_1 + c_5 N_5 + c_8 N_8 & H_2^y &= b_5 N_5 + b_8 N_8 \\
H_3^x &= b_5 N_5 + b_8 N_8 & H_3^y &= -N_1 + e_5 N_5 + e_8 N_8 \\
H_4^x &= 1.5\left(a_6 N_6 - a_5 N_5\right) & H_4^y &= 1.5\left(d_6 N_6 - d_5 N_5\right) \\
H_5^x &= -N_2 + c_6 N_6 + c_5 N_5 & H_5^y &= b_6 N_6 + b_5 N_5 \\
H_6^x &= b_6 N_6 + b_5 N_5 & H_6^y &= -N_2 + e_6 N_6 + e_5 N_5 \\
H_7^x &= 1.5\left(a_7 N_7 - a_6 N_6\right) & H_7^y &= 1.5\left(d_7 N_7 - d_6 N_6\right) \\
H_8^x &= -N_3 + c_7 N_7 + c_6 N_6 & H_8^y &= b_7 N_7 + b_6 N_6 \\
H_9^x &= b_7 N_7 + b_6 N_6 & H_9^y &= -N_3 + e_7 N_7 + e_6 N_6 \\
H_{10}^x &= 1.5\left(a_8 N_8 - a_7 N_7\right) & H_{10}^y &= 1.5\left(d_8 N_8 - d_7 N_7\right) \\
H_{11}^x &= -N_4 + c_8 N_8 + c_7 N_7 & H_{11}^y &= b_8 N_8 + b_7 N_7 \\
H_{12}^x &= b_8 N_8 + b_7 N_7 & H_{12}^y &= -N_4 + e_8 N_8 + e_7 N_7
\end{aligned}
\tag{3.64}
$$

in which

$$a_k = -\frac{x_{ij}}{l_{ij}^{\,2}} \tag{3.65}$$

$$b_k = \frac{3 x_{ij} y_{ij}}{4 l_{ij}^{\,2}} \tag{3.66}$$

$$c_k = \frac{\frac{1}{4} x_{ij}^{\ 2} - \frac{1}{2} y_{ij}^{\ 2}}{l_{ij}^{\ 2}} \tag{3.67}$$

$$d_k = -\frac{y_{ij}}{l_{ij}^{\ 2}} \tag{3.68}$$

$$e_k = \frac{-\frac{1}{2} x_{ij}^{\ 2} + \frac{1}{4} y_{ij}^{\ 2}}{l_{ij}^{\ 2}} \tag{3.69}$$

where $(k = 5,6,7,8)$ $(i = 1,2,3,4)$, $(j = 2,3,4,1)$ and $(ij = 12,23,34,41)$

3.4.1.3 Displacement control Incremental-iterative numerical strategies for nonlinear analysis

Within the context of structural analysis, iterative procedures similar to the Newton-Raphson method can be adapted to determine nonlinear load-displacement relations. For softening behavior, a procedure should involve displacement control. We have adopted a displacement control only algorithm (Batoz and Dhatt, 1979). For that purpose, the equations are cast into *n*+1dimensional space, where in addition to the *n* displacement parameters, a load-related parameter also appears as unknown. This requires an additional constraint equation to keep the number of unknowns as the original number *n*. The augmented incremental equations can be written in the form:

$$\left[\begin{array}{c|c} \mathbf{K}_i^{j-1} & -\mathbf{P}^{\text{ext}} \\ \hline \mathbf{a}_i^{j\,\mathrm{T}} & 0 \end{array}\right] \left\{\begin{array}{c} \delta\mathbf{d}_i^j \\ \hline \delta\lambda_i^j \end{array}\right\} = \left\{\begin{array}{c} \mathbf{r}_i^{j-1} \\ \hline \delta d_{ctrl\ i}^{\ j} \end{array}\right\} \tag{3.70}$$

where the vector *a* can be written as

$$\mathbf{a}_i^j = \langle 0 \quad \cdots \quad \underset{ctrl}{1} \quad \cdots \quad 0 \rangle^{\mathrm{T}} \tag{3.71}$$

Because of the size of nonlinear structural problems, the solution is generally sought in an incremental-iterative manner, where the subscript *i* indicates the increment number, and *j* indicates the iteration number. Due to the nature of the nonlinear structural problems, the internal forces are functions of the displacements; however, the internal forces are not necessarily in equilibrium with the external forces at each iteration. Thus, an unbalanced force is generated. The displacement and external loads are computed by adding the contributions from the previously converged equilibrium configuration to the incremental updates at the current j^{th} iteration of the current i^{th} increment. Similarly, the incremental updates at step *i* are computed by adding the contribution from the previous j-1^{th} iteration and iterative updates from the current j^{th} iteration. The nonlinear equations are then solved at each iteration within each step as shown in Fig. 3.17.

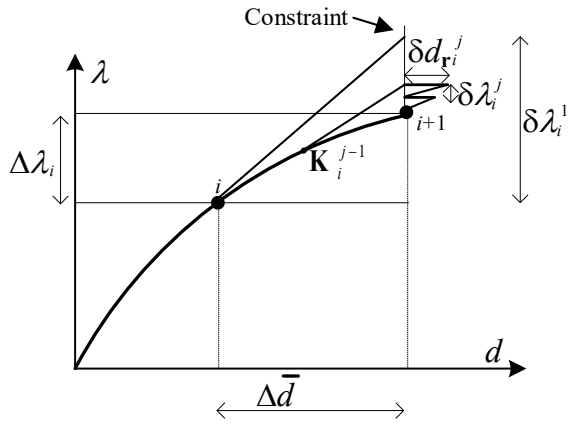

Fig.3.17 Iterative procedure under displacement control (Erkmen, 2019)

3.4.1.4 Multi-point constraint (MPC)

The idea for Multi-point constraint (MPC) is to introduce equations that relate DOFs into different nodes that may even be some distance between them, i.e., the translation or rotation of a node called slave is related to the other node called master. To illustrate the idea, an imaginary rigid

body can be introduced to help nodes relate to each other. The equations introduced as MPC can be derived using the simple kinematic rules of a rigid body movement. After assuming that both nodes 1 and 2 are perfectly connected to the rigid body with a reference point of 3 (nodes 1 and 2 are slaves and node 3 is master), movements related to nodes 1 and 2 are calculated as below.

$$d_1 = q_1 + \beta q_3 \tag{3.72}$$

$$d_2 = q_2 \tag{3.73}$$

$$d_3 = q_3 \tag{3.74}$$

$$d_4 = q_1 \tag{3.75}$$

$$d_5 = q_2 + \alpha q_3 \tag{3.76}$$

$$d_6 = q_3 \tag{3.77}$$

Fig.3.18 graphically presents the relationship between the nodes using a rigid body.

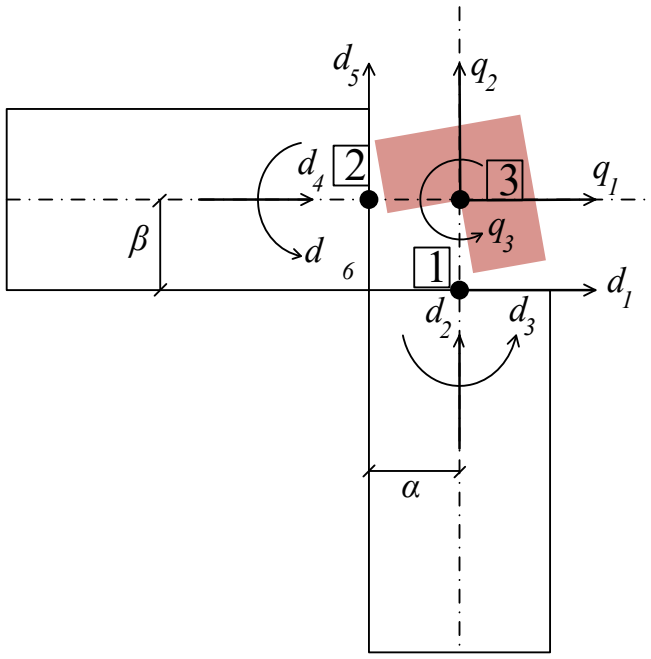

Fig.3.18 Rigid body used to introduce equations (Liu et al. 2014)

3.4.2 Imperfections

Initial imperfections are always present in steel structural members (Shayan et al. 2014). The buckling of thin-walled shells have extreme sensitivity to initial imperfections (Sadovsky and Krivacek, 2020). These imperfections are defined as derivations from considered perfect shape and material properties, as well as, assigned boundary conditions and applied loads. Geometric imperfection modelling in frame structures have to be considered since not only the magnitude of the imperfection but also its pattern influences the frame structure. For the purpose of implementation of imperfections in the structure, the elastic buckling analysis (eigenvalue analysis) can be a good alternative. However, the plastic deformation is also important in the final failure. In the Fig. 3.19, the first three buckling modes of a simply supported axially loaded column is presented.

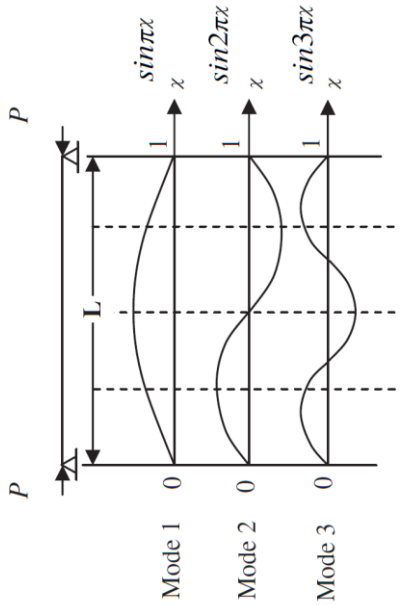

Fig.3.19 First three buckling modes of a simply supported axially loaded column

Initial imperfections have to be considered before the analysis starts. The procedure of considering imperfection is presented below in Fig.3.20:

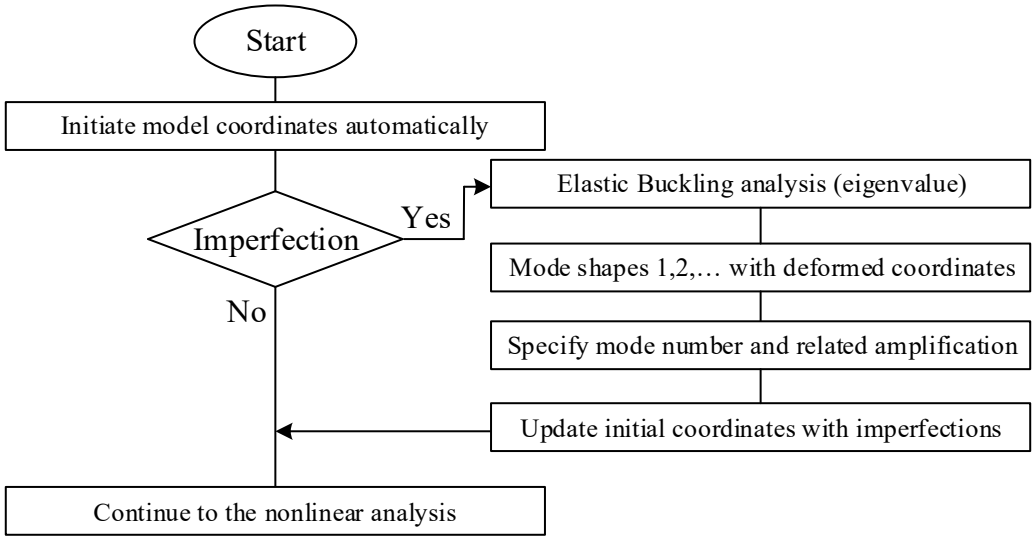

Fig.3.20 Flowchart for imperfection implementation

3.4.3 Buckling of strips about their weak axis-study of the plate component as a validation of shell element

Euler column buckling problem under simply supported boundary conditions is considered for validation purposes. The column is under constant compressive force due to a typical load as shown in Fig. 3.21 a and end restraint conditions are described in Fig. 3.21 b.

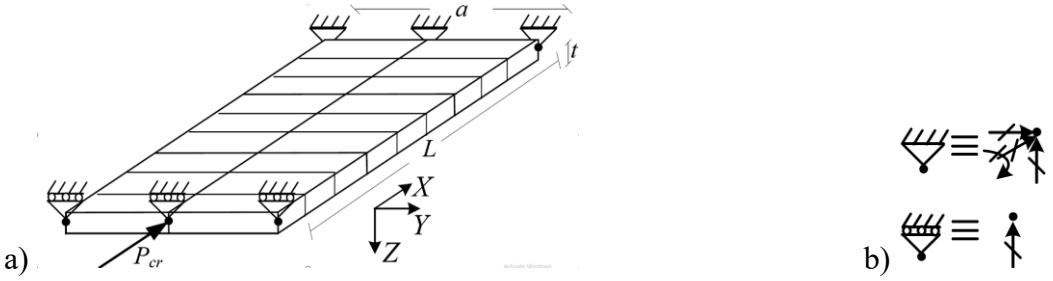

Fig. 3.21a) Supports and loading point b) Support definition

The analyses were made for L=1000 mm, a=200 mm and the thickness t=10 mm, for which the buckling loads can be obtained from Eq.(3.77). For the modelling purpose the mesh used as shown in the picture is 9x2.

$$P_{cr} = \frac{\pi^2 EI}{l^2} \tag{3.78}$$

Table 3.1 Buckling load comparison between model and formula

Method	Buckling load (kN)	Error (%)
Formula	2202.56	
Element	2223.93	0.0097 %

CHAPTER 4: FRAME ANALYSIS USING FINITE ELEMENT CONSIDERING FATIGUE DAMAGE

In this chapter, modelling information regarding material, element characteristics and loading protocol is presented. In the first stage, a cantilever beam is used for verification of the modelling and results. Then, for the mentioned cantilever beam, a mesh sensitivity analysis is conducted. Then, the mainframe used in the study is introduced, and the procedure of the analysis is presented.

4.1 Cantilever Beam

4.1.1 Modelling and verification

To verify the modelling technique and capability of the shell element used in the study, the experimental test results obtained for a cantilever I-shape beam selected from the literature (Engelhardt et al. 1994) were used. In the study, a quasi-static cyclic displacement loading is applied to the cantilever beam. The study is conducted on an I-shaped beam of a moment resisting frame (MRF) and the beam dimensions and mechanical properties corresponding to specimen 7A in Engelhardt et al. (1994) are presented in Table 4.1. A schematic setup of experimental test is presented in the Fig.4.1. The effective length of the beam specimen is calculated as (Bosco and Tirca, 2017).

$$L_v = L - \frac{d_c}{2} - l_c \tag{4.1}$$

The finite element modelling of the cantilever beam is presented in Fig.4.2 where is shown the initial mesh generated for the study.

Tab.4.1 Mechanical properties of the specimen 7A as per Engelhardt et al. (1994)

Specimen number	Cross-section	F_y Flange (MPa)	F_y Web (MPa)	Elasticity modulus (MPa)	L_v (mm)
7A	W36 × 150	301.3	362.3	2.1×10^5	2985

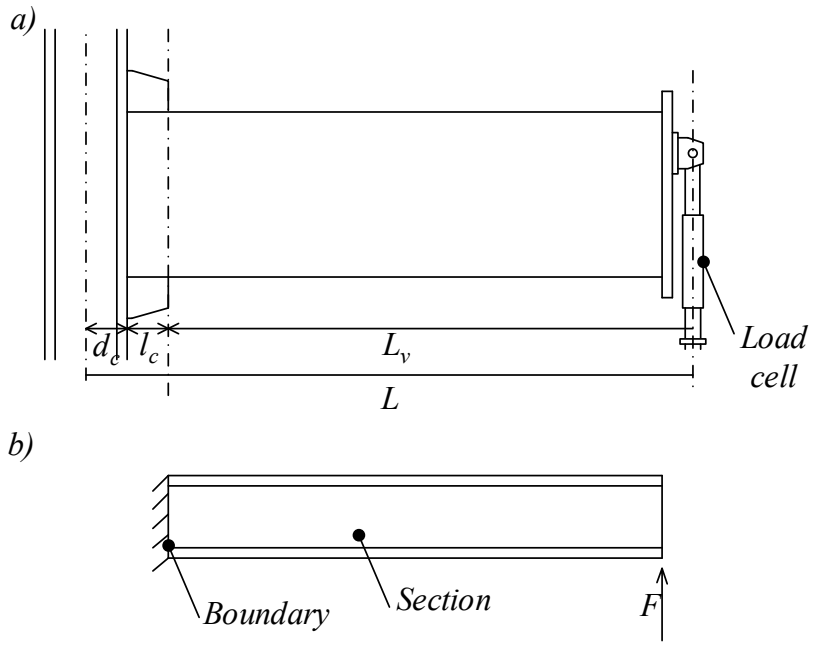

Fig.4.1 Cantilever beam a) Experimental test setup (Bosco and Tirca, 2017) b) modelling of I-shaped specimen in the setup

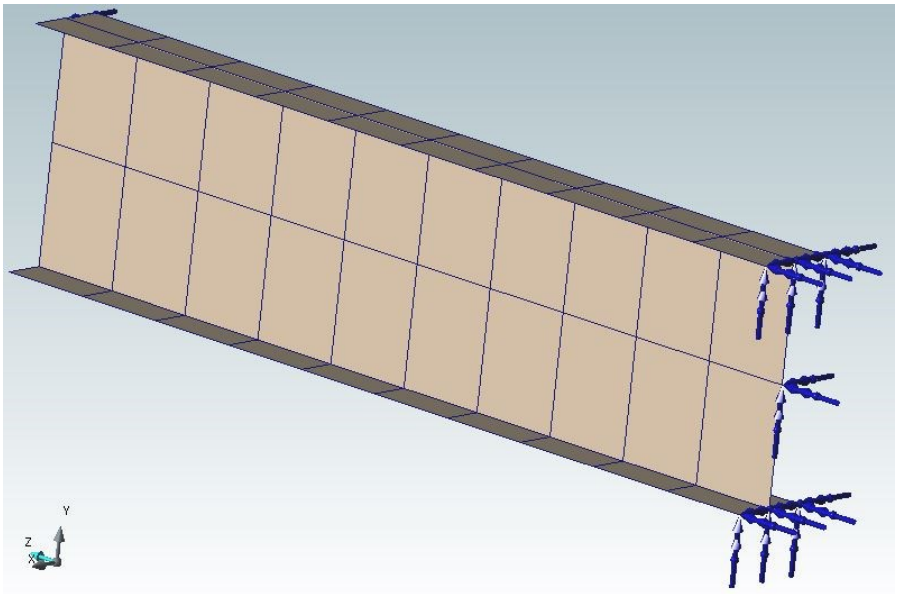

Fig.4.2 Finite element modelling of the cantilever beam in the setup using 60-element model

On the fixed side of the model, all of the nodes are fixed for rotation and translation. To capture the beam element behaviour, the nodes, where the load is applied, are banned in side translation to avoid lateral-torsional buckling. As seen in Fig.4.2, the model is divided into 10 longitudinal elements and the cross-section is provided in Fig.4.3.

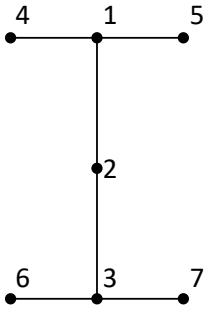

Fig.4.3 Cross-section mesh for cantilever beam

The beam theory is applied in the first case to capture only the flexural behaviour, and for this purpose, using the multi-point constraint (MPC) method, the condition of “plane surface stays

plane" is satisfied. The Fig.4.4 presents the MPC for different degrees of freedom, with the master point of node number 2 and other nodes as slave nodes.

X-direction

Y-direction

Z-direction

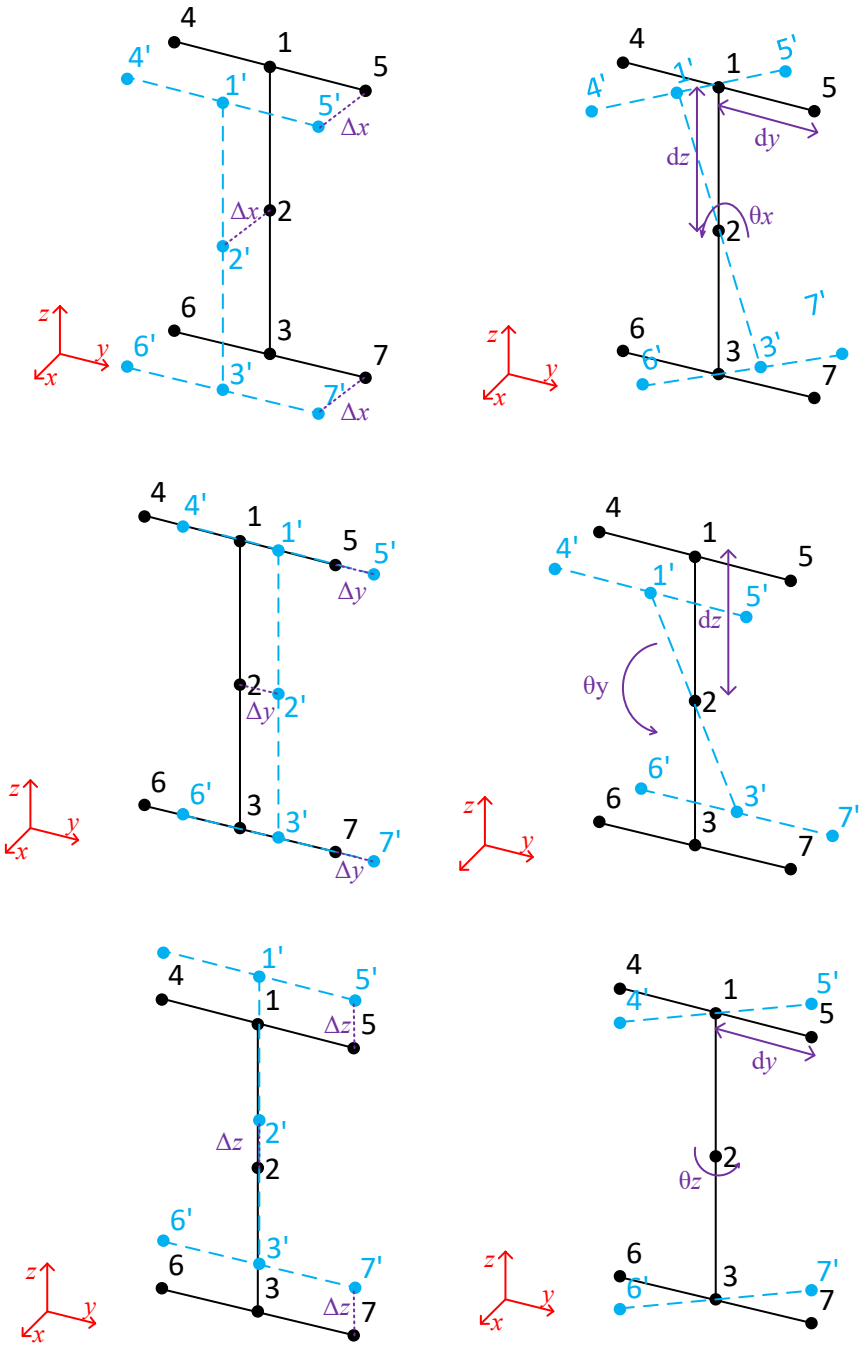

Fig.4.4 MPC for different degrees of freedom with the master point of node number 2 and other nodes as slave.

The quasi-static cyclic displacement loading protocol is presented in the Fig.4.5.

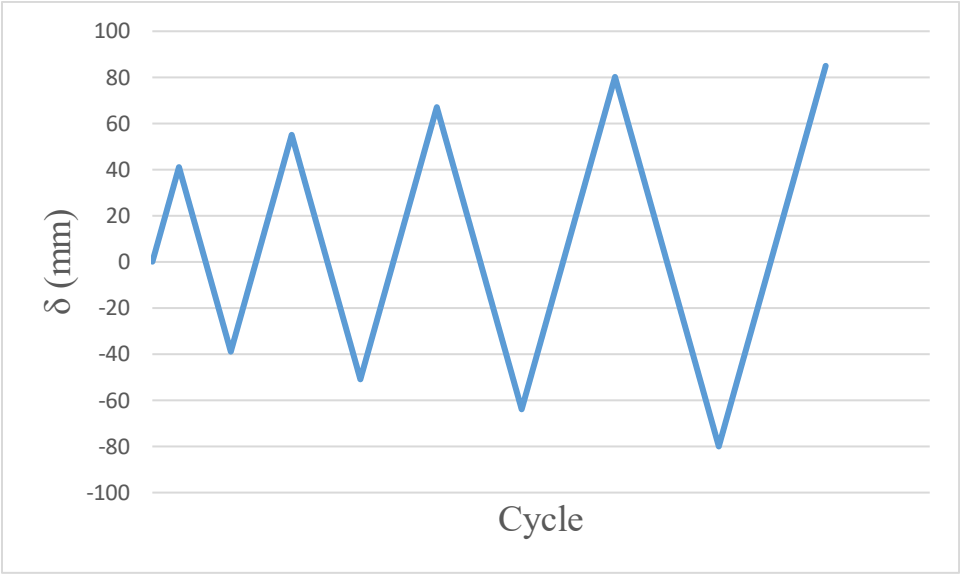

Fig.4.5 The quasi-static cyclic displacement loading protocol

For the nonlinear analysis, as mentioned before, the Von-Misses yield criteria is applied. The hardening function values used in Eq.3.47 and Eq.3.48are $K_0 = 100MPa, Hs = 200MPa$ with $\xi_t = 0.1MPa$. The results of nonlinear analysis for the first case study, conducted on cantilever beam loaded as indicated in Fig.4.5 is presented in Fig.5.6 against the hysteresis loops obtained by Bosco and Tirca (2017). The beam theory without stiffness degradation due to fatigue loaded is applied in shell elements.

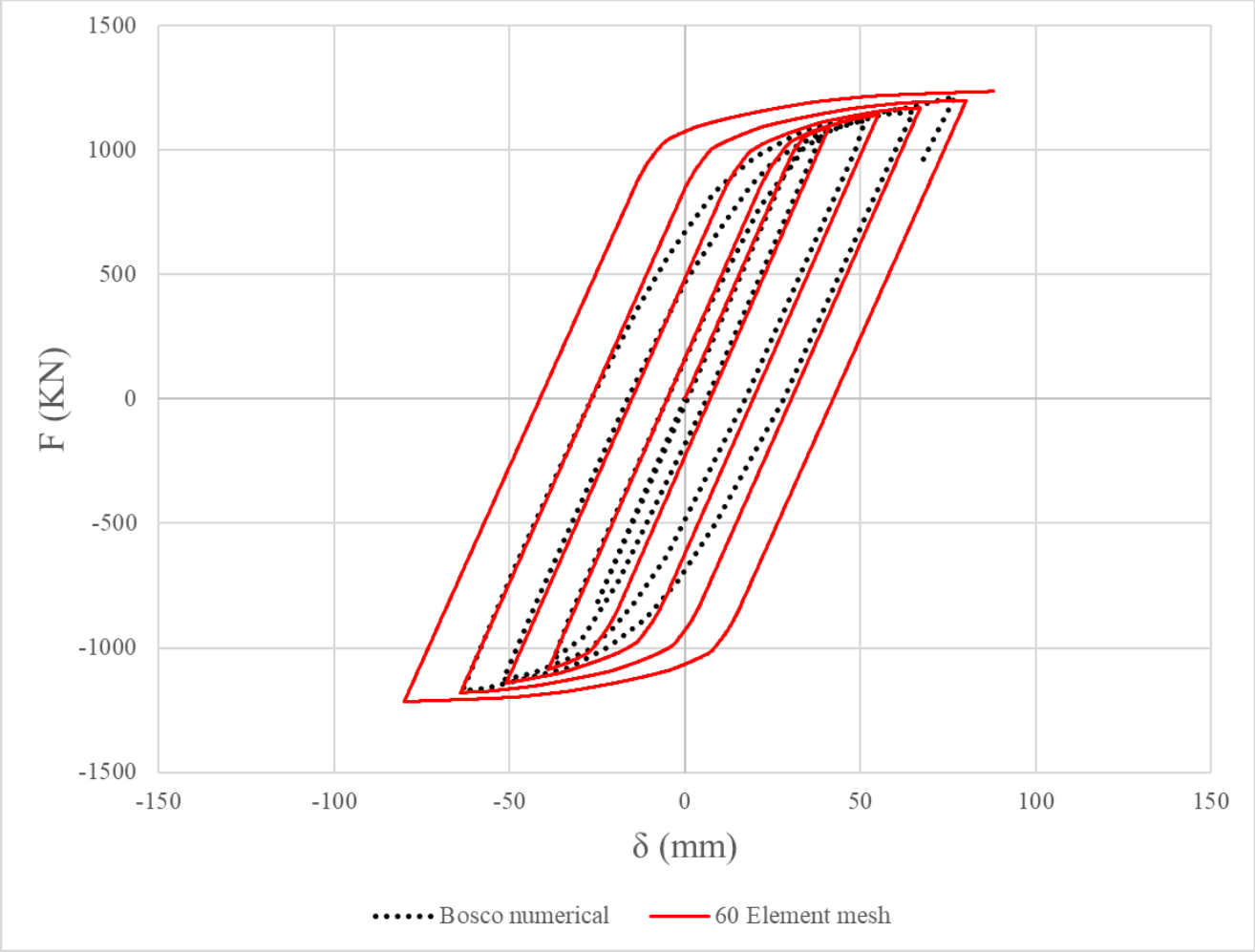

Fig.4.6 Hysteresis loops from nonlinear analysis using beam theory in shell element without stiffness degradation against the results obtained by Bosco and Tirca 2017

The Fig.4.6 shows a good accordance between the model and the literature. There are some parts that two figures do not overlap and it explains differenced between two modelling techniques.

4.1.2 Elastic Identical Solution

To investigate the accuracy of the element in resulting tip point deformation, the elastic identical solution is compared with the result obtained from Finite element method. The results of comparison in presented in the Table 4.2.

Table 4.2 Identical and present modelling solution comparison for cantilever beam

Method	Displacement (mm)	Error
Exact solution	87.504	
Present modelling	87.799	0.337 %

4.1.3 Mesh sensitivity analysis

For mesh sensitivity analysis, two cases with 60-element presented in the previous section and a 480-element model were considered. In Fig.4.7, the 480-element model is presented. The values for the analysis are the same, and MPCs are applied to master node which is the midpoint of the web as before, and results show a good match. In Fig. 4.8, the comparison between the 60-element model and the 480-element model is presented.

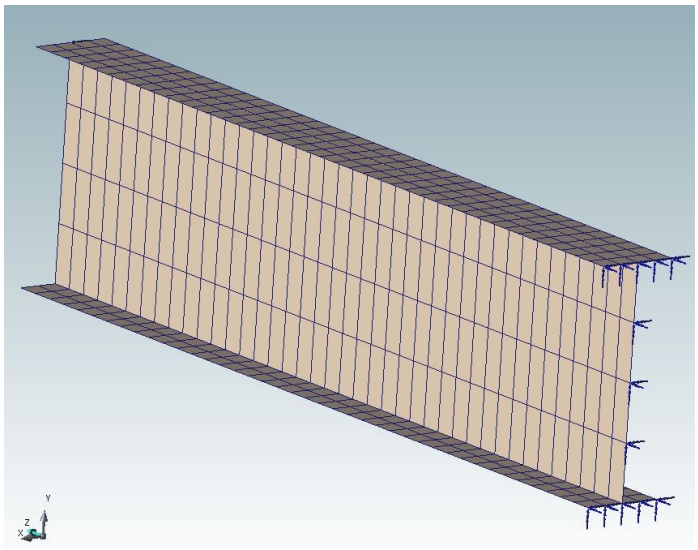

Fig.4.7 Finite element modelling of the cantilever beam in the setup considering 480-element model

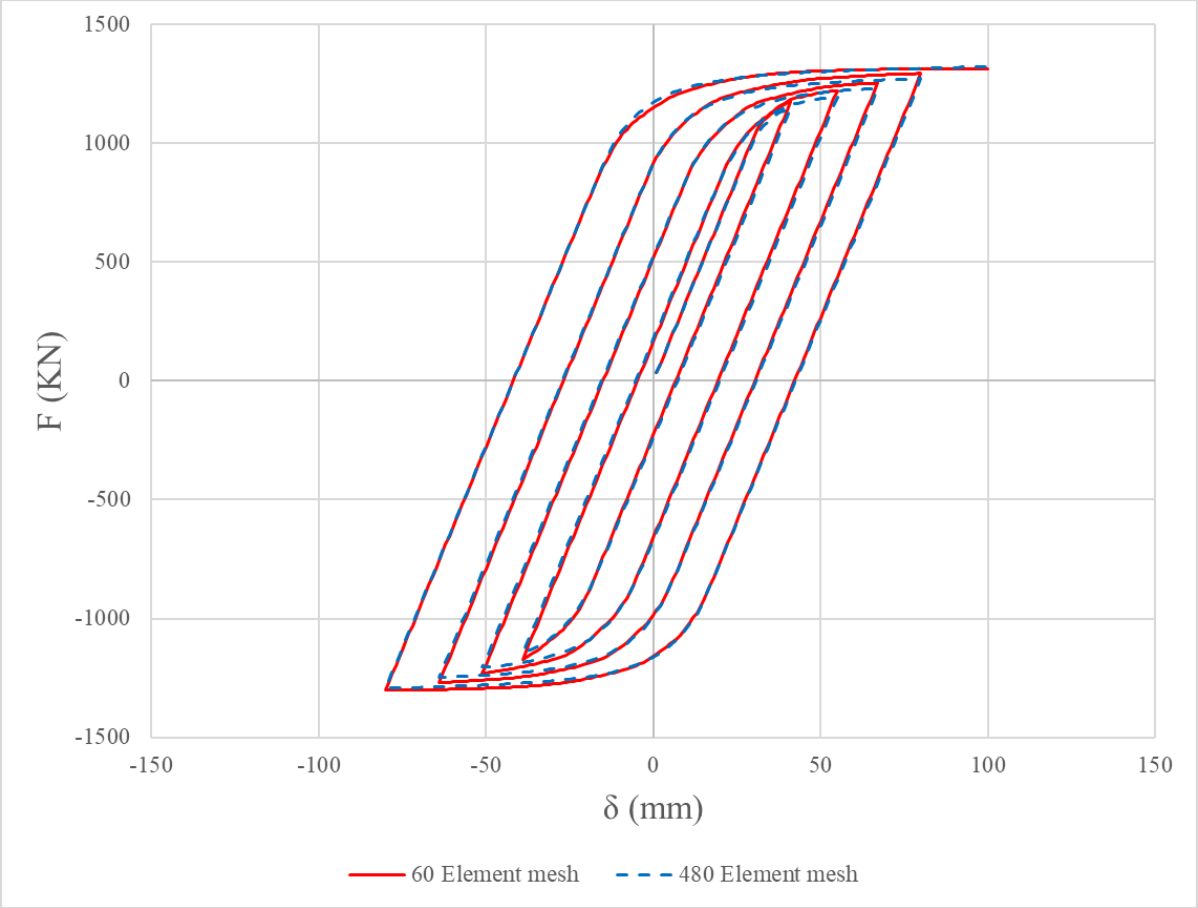

Fig.4.8 Hysteresis loops using beam theory in shell element without stiffness degradation considering 60-element model vs 480-element model

As resulted from Fig. 4.8, using 60-element vs. 480-element the hysteresis loops overlap.

4.2 Frame Analysis

A one-bay single-story moment frame structure is used to investigate different types of failure modes when the members are modelled using shell elements. In this example, columns and beam have cross-sections of W14x176 (W360x162) and W21x44 (W530x66), and the beam-column connection is assumed rigid by assigning thickness of 45mm to the elements inside panel zone. The dimensions of the above sections are presented in Table 4.3. As shown in Fig. 4.9, the length and the height of the frame are 6.00 m and 3.40 m, respectively. Monotonic and cyclic

displacement-load pushover analysis is performed using nonlinear analysis discussed in previous sections.

Table 4.3 Dimensions and characteristics of beam and columns sections

Element	Area mm^2	I_x 10^3 mm^3	Z_x 10^3 mm^3	I_y 10^3 mm^3	Z_y 10^3 mm^3	d mm	b mm	t_f mm	t_w mm
W530x66	8390	351	1560	8.57	166	525	165	11.4	8.9
W360x162	20600	515	3140	186	1520	364	371	21.8	13.3

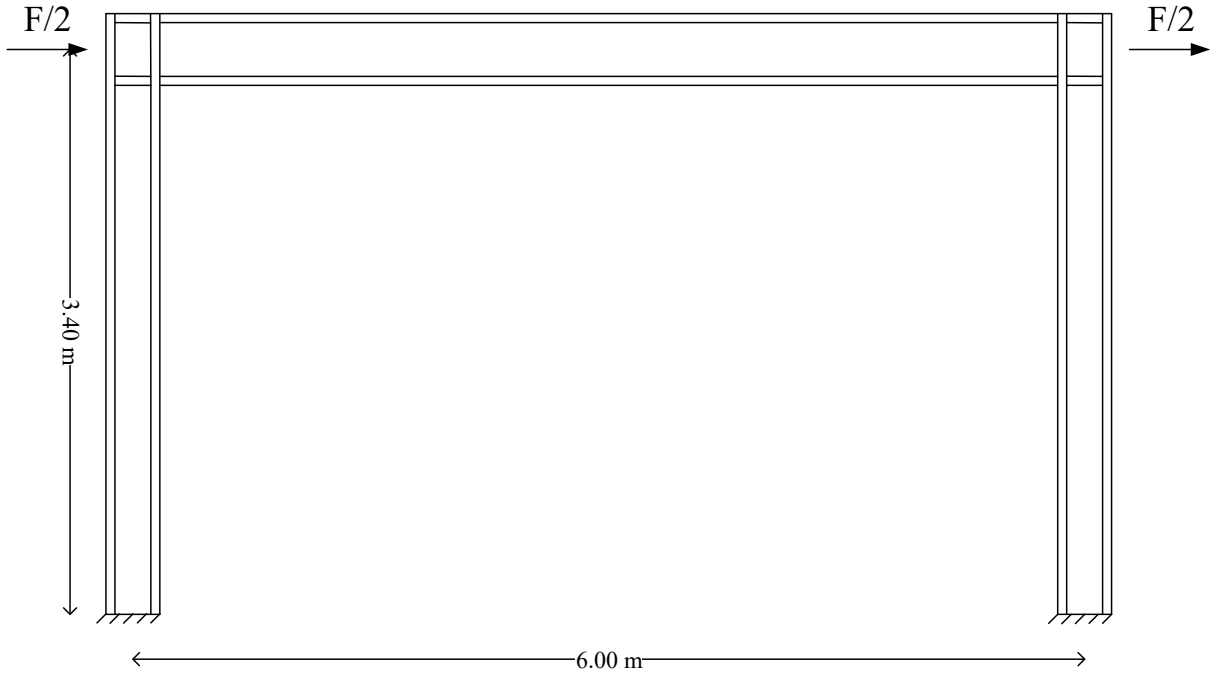

Fig.4.9 The geometry of investigated one –storey moment frame

4.2.1 Modelling

For modelling the frame, columns and beam have been meshed as shown in Fig. 4.10. The longitudinal mesh is 20 elements for both beam and columns. The number of shell elements considered is 140 element for beam and each column. The section is meshed as shown in Fig.4.3.

There is a panel zone in the place of beam-column connection consisting of 20 elements. The bottom nodes of columns are restricted in all 6 DOFs. The frame is loaded laterally on both sides.

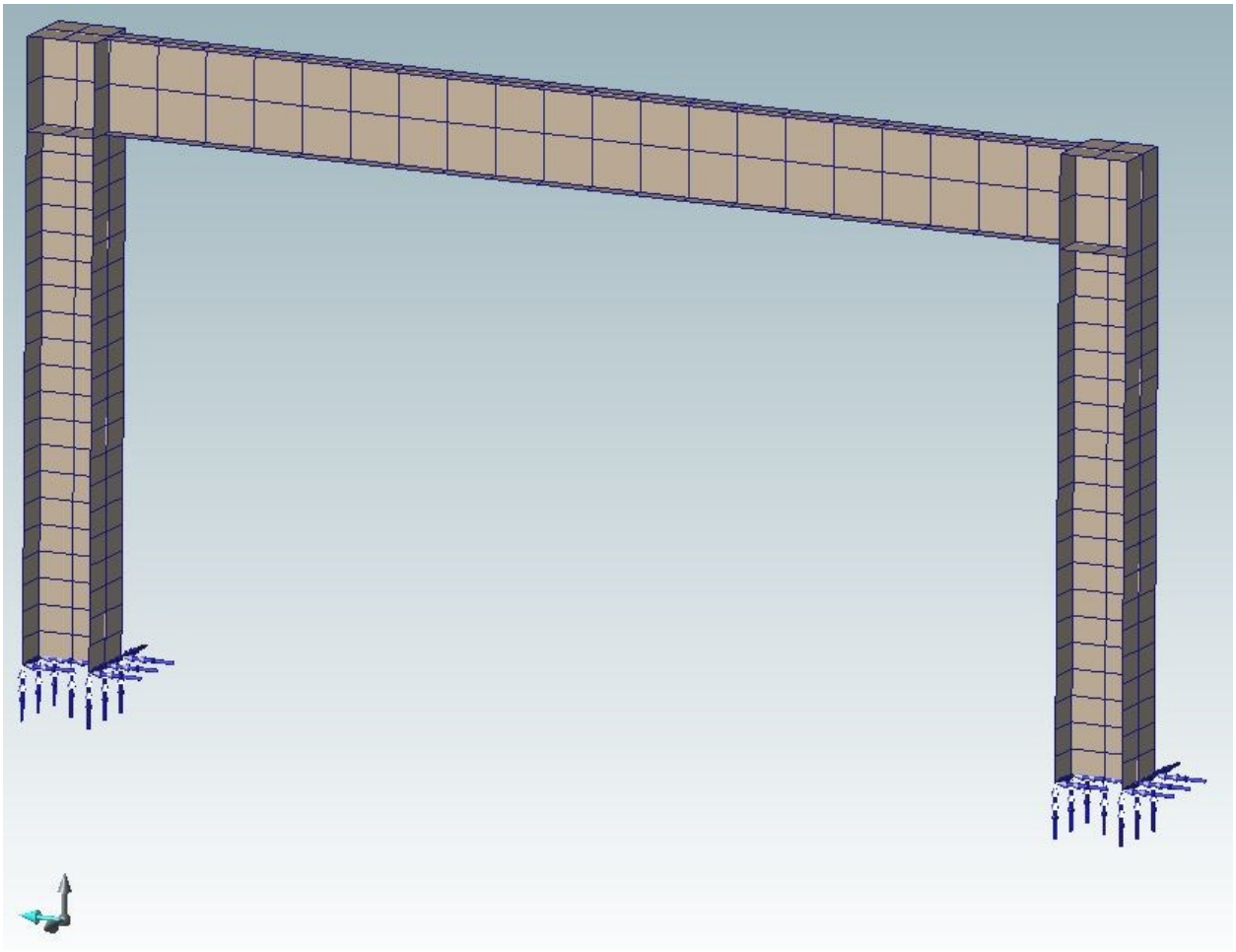

Fig.4.10 Frame model mesh

4.2.2 Multi-point constraint

MPCs are used in two different places in the frame. First, the connections are generated separately, then, they are connected to the main elements of the beam and columns using MPCs. The benefit of this technique is that the columns and beam can have different dimensions and different mesh. The connection with MPCs is presented in the Fig.4.11.

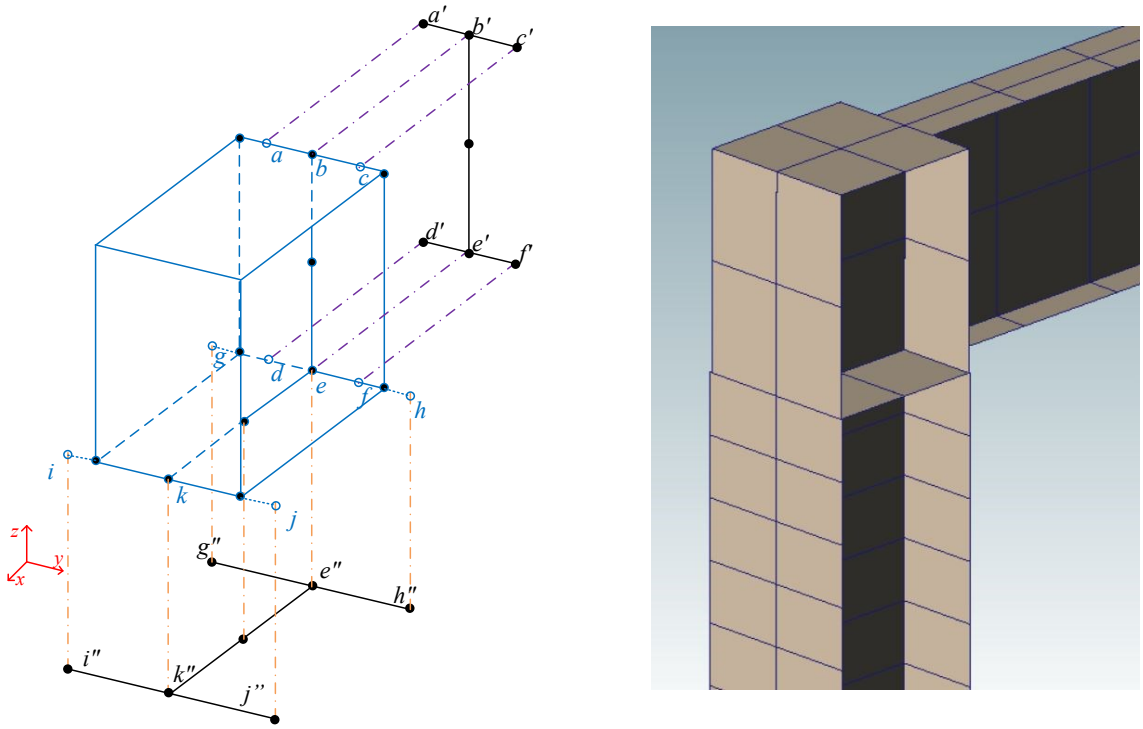

a) b)

Fig.4.11 MPCs applied to the connection

In this study, nodes *a'* to *f'* are considered as nodes present on the beam element and nodes *e''* to *k''* are considered as nodes present on the column element. For connecting these nodes to the connection box, the nodes *a* to *c* are slaves of the nodes *a'* to *f'* in all three dimension translations and rotations, and nodes *e''* to *k''* are slaves of nodes *g* to *j* presented in shape. The main benefit of generating separate mesh assembling the components using MPC method is that it can connect sections with different number of meshes to the connection. This means that there is a capability in using this type of modelling where a different number of meshes can be assigned to beam, column, and the connection in the panel zone. This capability used in modelling makes it easier to assign smaller mesh size in the places that is important to have precise results.

4.2.3 Beam and column connections including the panel zone

To investigate the behaviour in the structural elements, the beam-column connection is made rigid using higher thickness that has the capability to rotate and translate on the side that is connected to cross section. It is also possible to investigate the behaviour of panel zone, but it is not the priority of this study.

4.2.4 Fatigue damage implementation

For implementing fatigue damage, the value for α in Eq.3.42 is 0.006, x_1, and x_2 are considered as 25.0 $\frac{mm}{cycle(MPa)^{x_2}}$ and 0.45, respectively. For the hardening parameters presented in Eq.3.46 and Eq.3.47 are $K_0 = 0\ MPa$, $Hs = 0\ MPa$ $Hss = 0.09\,MPa$, $\xi_t = 10.0\,MPa$.

For the steel material for web and flanges on both beam and column, Fy = 317.1 MPa.

4.2.5 Loading protocol

A pushover analysis and a quasi-static cyclic displacement load are applied to the model in the analysis. A displacement control pushover analysis is performed in the first case. To investigate the fatigue effect in the model, the considered cyclic loading is also applied as a separate case presented in Fig.4.12.

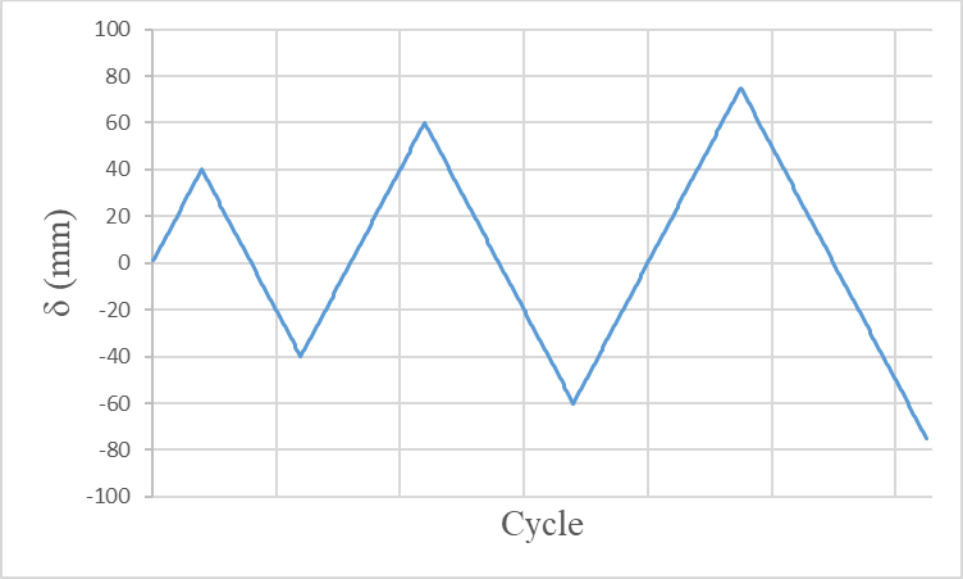

Fig.4.12 Cyclic load implemented in the analysis

4.2.6 Modelled cases

4.2.6.1 Case 1 (Beam element)

Using MPCs explained in Fig.4.4, the mid node on the web is the master of the other nodes to make the beam cross-section stay on the plane surface. Then, boundaries are applied to restrict the side translation in the model. The conditions imposed are to capture only flexural deformation in the beam and column of the model. In this model, no imperfection is implemented.

4.2.6.2 Case 2 (MPCs assigned only)

In the model, side translation boundaries are lifted to allow lateral deformations and only MPCs are present in the model. Using the MPCs, modal analysis is performed, and the first buckling mode is implemented as an imperfection.

4.2.6.3 Case 3

To capture local buckling behaviour, another modal analysis is performed after lifting all the restrictions. In this case, no MPC is implemented, and side translation boundaries are present in

the model. The MPCs used in connections to transfer the loads and displacements from beam to columns are still present. The first mode deformed shape is imposed as the imperfection in the system.

4.2.7 Modal analysis

Modal analysis is performed to implement the imperfections in the model. The mode shape that is considered as the imperfection in the analysis is the first buckling mode. In multi-story buildings, the effect of higher modes can be easily taken into account. This kind of imperfection implementation can lead to the lateral-torsional buckling and local buckling modes. If the imperfection is not imposed in the model, the stiffness matrix in the deformed point without any direct loading will face a problem.

Local and global deformation modes can also be captured using shell eigenvalue analysis. As presented in Fig.4.13, Fig. 4.14 and Fig.4.15, the most probable mode shapes are related to the restrictions applied in modelling. The mode shapes are implemented as imperfection in the nonlinear analysis.

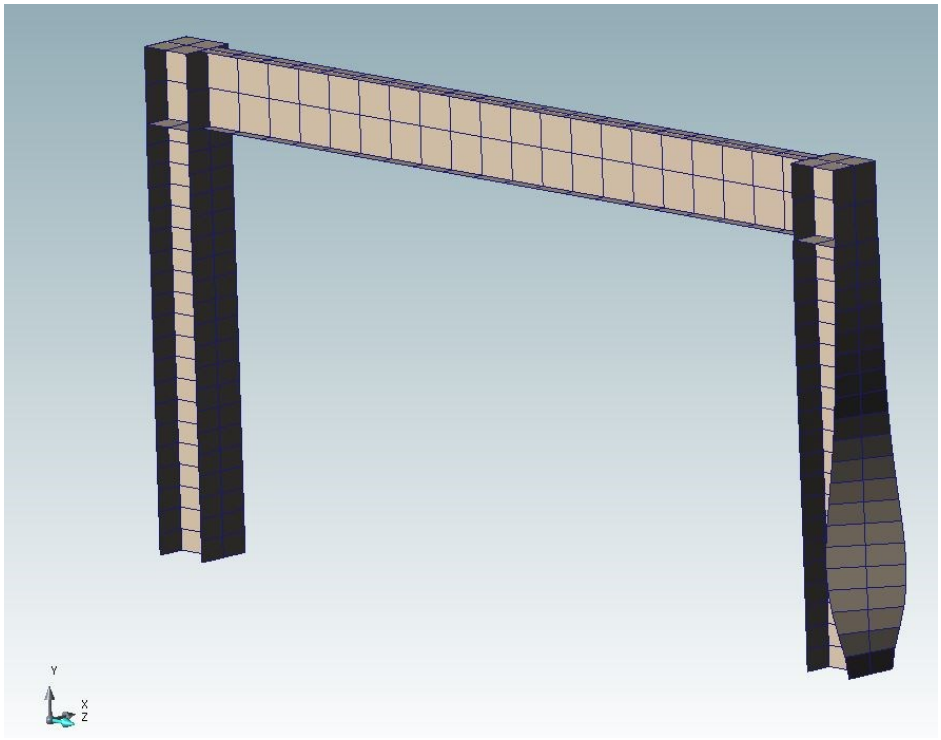

Fig.4.13 First buckling mode shape for Case 1 modelling

In Case 1 modelling, the shell element is forced to behave like beam element by implementing MPCs to cross-section surface forced to stay plane and by restricting the side translation, the lateral deformations are eliminated. The Case 2 is similar to Case 1 but side translation restrictions are lifted. It is shown in Fig.4.14 and Fig.4.15 as first buckling mode, the restrictions in beam section do not allow the mode shape to show any deformations. Therefore, the column, which has no restriction, is subjected to twist as the first mode, although there is a minor lateral deformation recorded in Case 2.

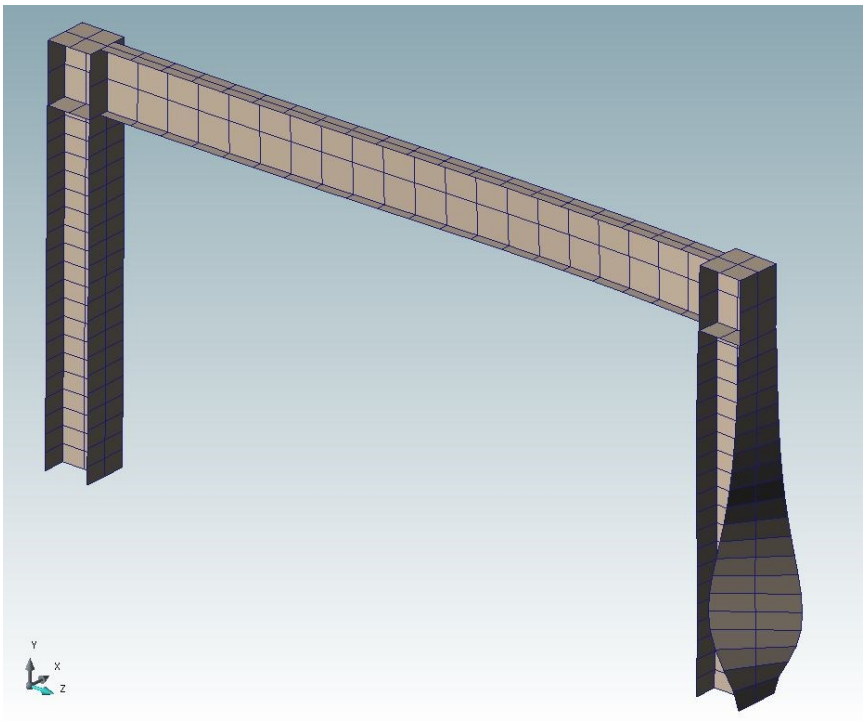

Fig.4.14 First buckling mode shape for Case 2 modelling

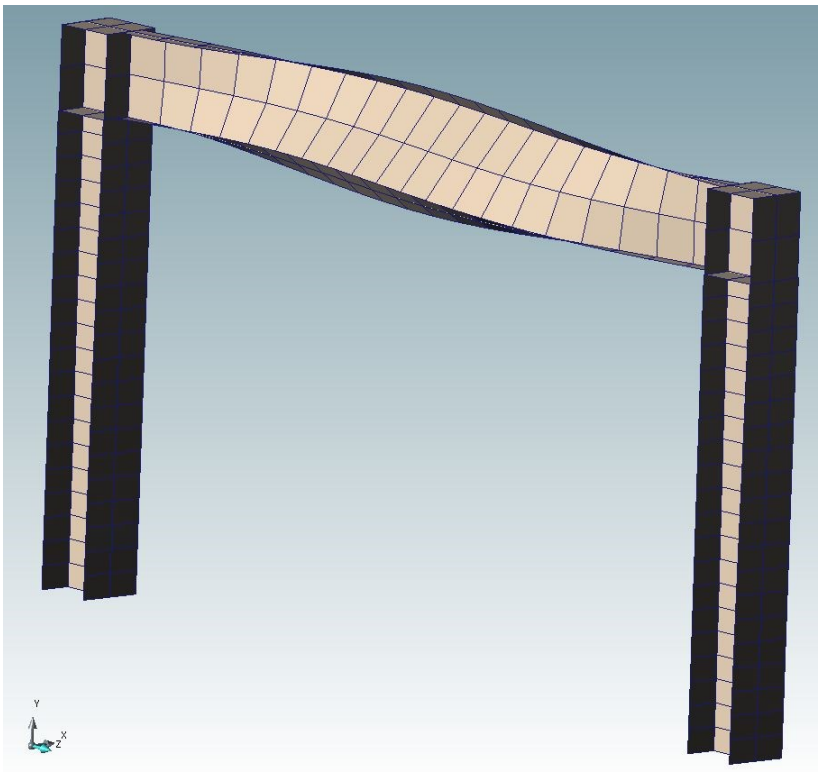

Fig.4.15 First buckling mode shape for Case 3 modelling

4.2.8 Nonlinear analysis

To challenge the capability of the model built base on finite element, three different analysis are consucted implementing various restrictions. To investigate the model's capability, the study based on beam theory (plane surface stays plane) is performed. Then, by eliminating some restrictions, an analysis to capture lateral-torsional buckling is also conducted. By eliminating the remaining restrictions, the capability of the model in capturing local buckling is investigated.

The displacements due to the loading are presented in Fig. 4.16 to Fig.4.18. The main goal of this analysis is to investigate the capability of shell modelling thin-walled structures under different loading with different restrictions. The implemented fatigue phenomena also add extra value to the research. Modelling techniques used in this study show that the shell element can be restricted to capture responses using the beam element as well.

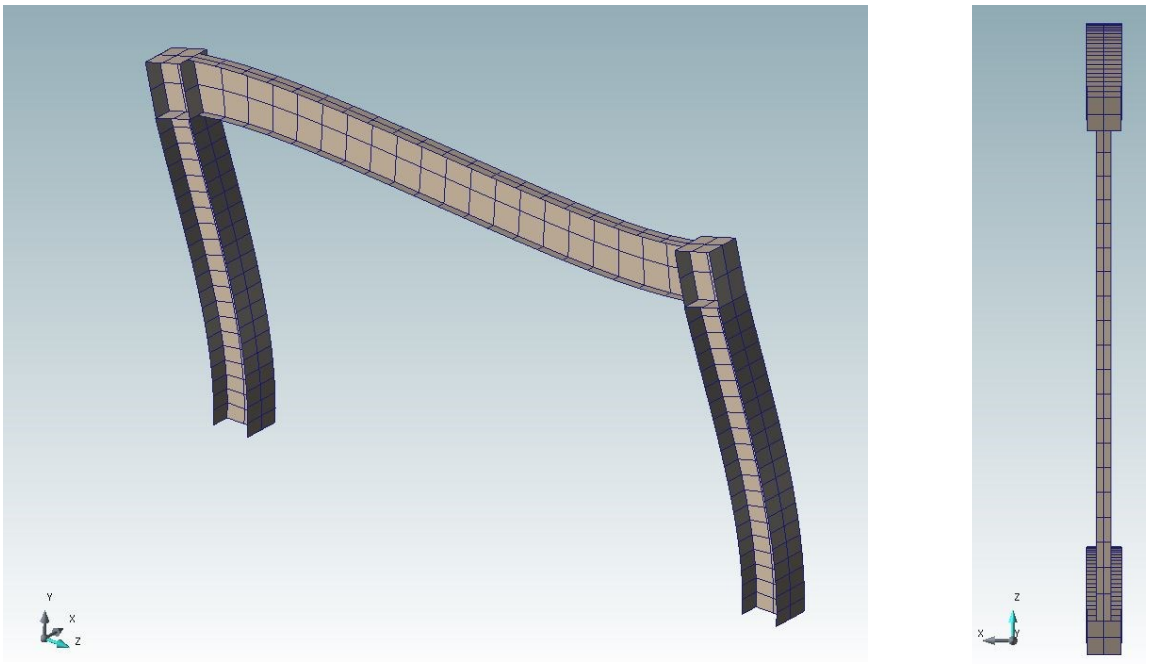

a) b)

Fig.4.16 Deformed shape for nonlinear analysis for Case 1 modelling

In the case of keeping cross section surface plane and restricting side translation, the shell element behaves as beam element and deform like beam element. In this case, only flexural deformations can be captured as shown in the picture. In Fig.4.16b there is no lateral deformation of the beam. Differences of the deformation in Case 2 and 3 are presented in Fig.4.17 and Fig.4.18. In Case 2, the cross-section surface stays plane as mentioned before but compared to Case 1, the side translation restrictions are lifted so the beam element can laterally be deformed or twisted. As shown in Fig.4.17b, the top view shows the lateral deformation in the beam element. In Case 3 all restrictions such as MPCs and lateral restrictions are lifted and the change is shown in Fig.4.18b.

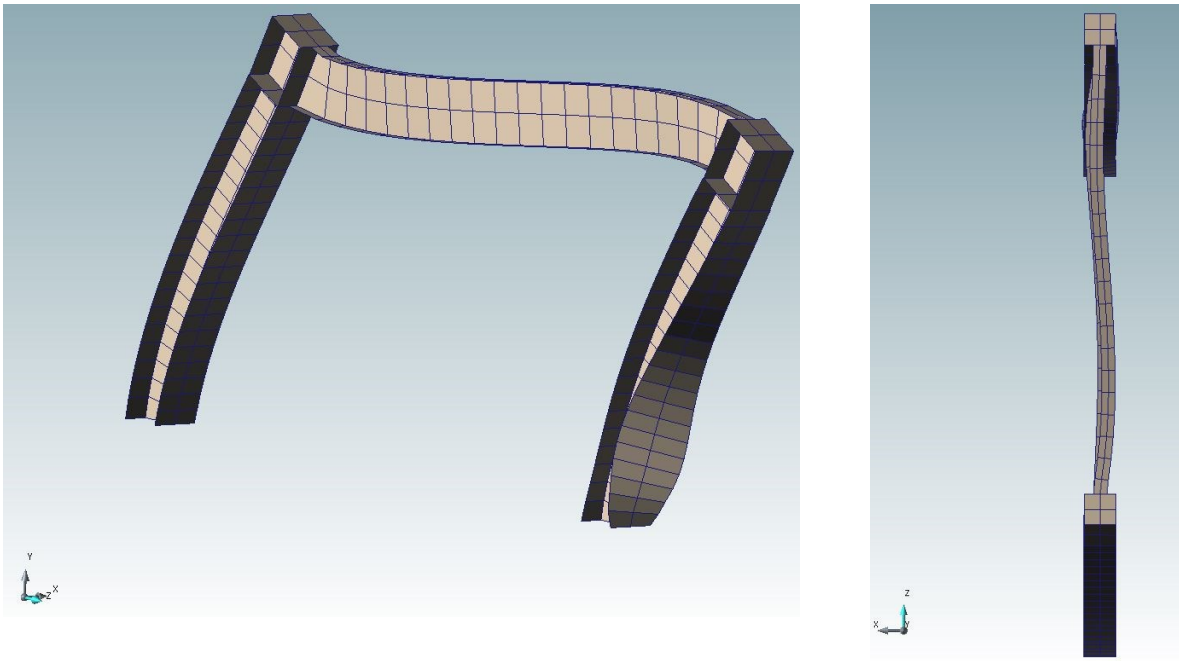

a) b)

Fig.4.17 Deformed shape for nonlinear analysis for Case 2 modelling

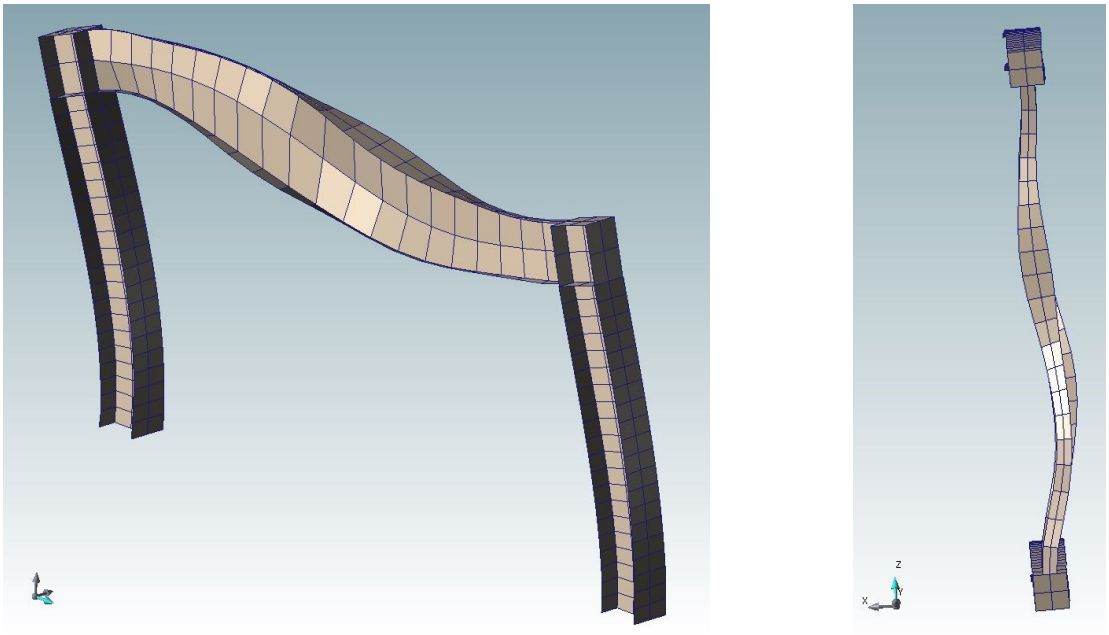

a) b)

Fig.4.18 Deformed shape for nonlinear analysis for Case 3 modelling

By comparing the results of these cases, it can be understood that shell element can capture other local behaviour such as partial plastic model, local deformations, etc.

CHAPTER 5: CASE STUDY RESULTS

5.1 Pushover Analysis

Displacement-control pushover analysis can be applied to models presented in the previous Chapter. The results presented in Fig.5.1 show that eliminating the restrictions in the analysis it can lead to different behavioural types as presented in previous sections. These behavioral types are also able to exhibit plasticity in earlier stages. The load-displacement curves presented in Fig.5.1 show the response according to Case 1 (beam element), Case 2 (model with MPCs assigned only but without side translation restrictions) and Case 3 (local, without MPCs and side translation restrictions allowing to capture local buckling). In all cases, the first mode of the related models was used as initial imperfection with the amplification factor of 2000.

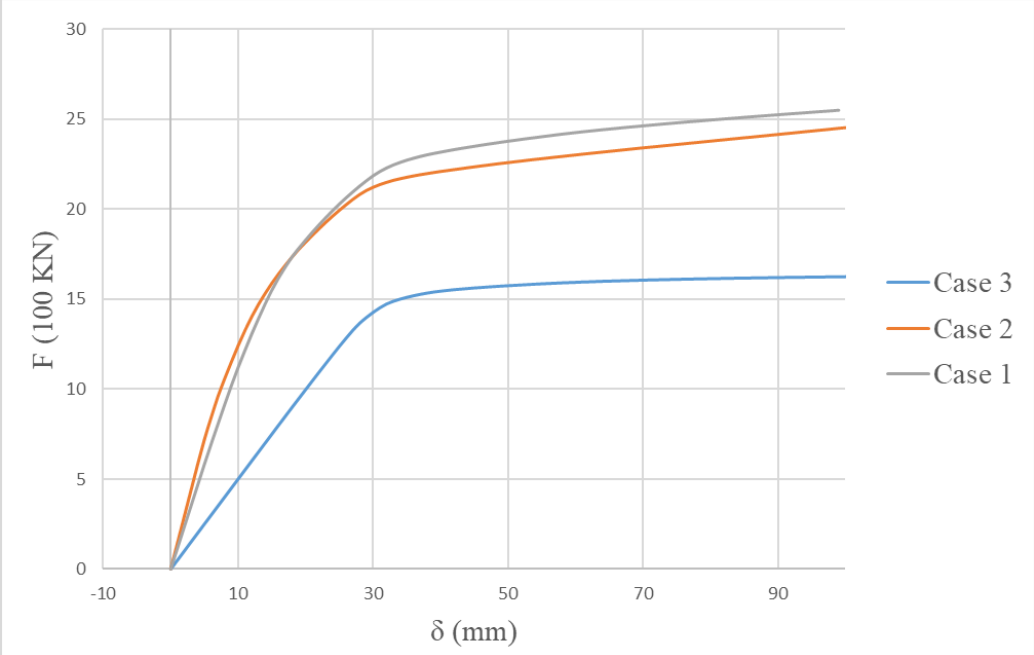

Fig.5.1 Pushover analysis result using displacement control

5.2 Cyclic Pushover Analysis

As mentioned before, the fatigue effect is caused by cyclic loading. Therefore, to compare the element functionality in capturing fatigue, the cyclic pushover is performed. In the below sections, the comparison of different cases are provided.

5.2.1 Frame analysis under cyclic pushover analysis without considering fatigue

Cyclic pushover analysis is performed to investigate the capability of the element in capturing cyclic behaviour. This type of analysis shows that local buckling can lead to plasticity in earlier stages. Considering the cyclic load presented in Fig. 5.2a, the hysteresis loops of the frame without considering the fatigue effect are presented in Fig 5.2b.

a)

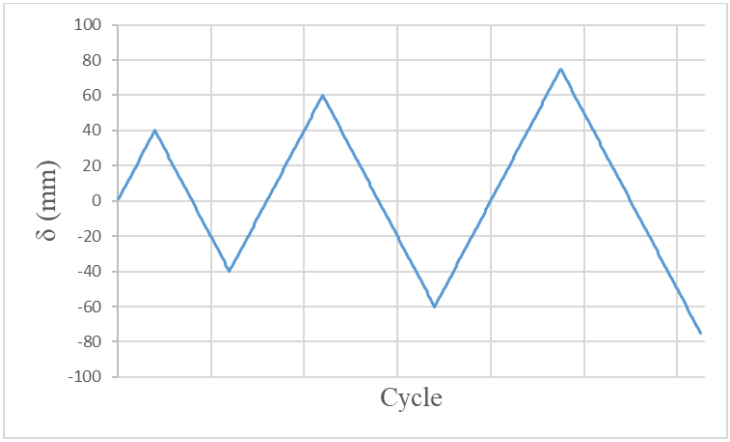

b)

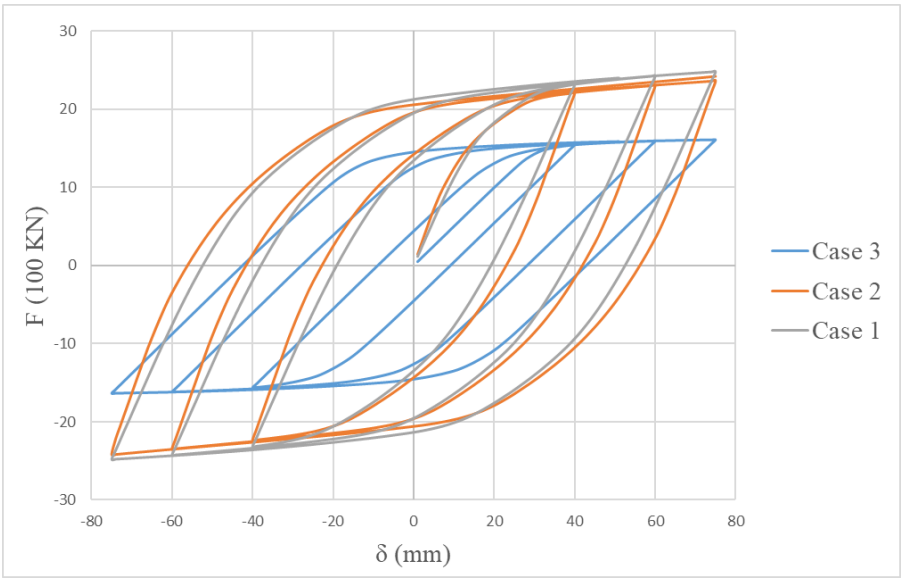

Fig.5.2 Frame response under quasi-static cyclic loading a) Quasi-static cyclic loading, b) Hysteresis loops of Cases 1, 2, and 3 resulted from cyclic-pushover analysis without considering fatigue

It is shown in Fig.5.2b, that the model in Case 3 is deformed under lower load when compared to Cases 1 and 2.

5.2.2 Frame analysis under cyclic pushover analysis considering fatigue

To investigate the capability of the shell element in thin-walled structural sections to capture other behavioral types, the cyclic pushover analysis considering fatigue effect is performed. The same type of quasi-cyclic cyclic loading as presented in Fig. 5.2a is considered and the hysteresis loops resulted for models developed for Cases 1, 2 and 3 are presented in Fig.5.3. As depicted, the damage related to fatigue has a large impact on material behaviour. The elasticity modulus and also the plasticity yield condition is impacted in the cases that fatigue damage is considered.

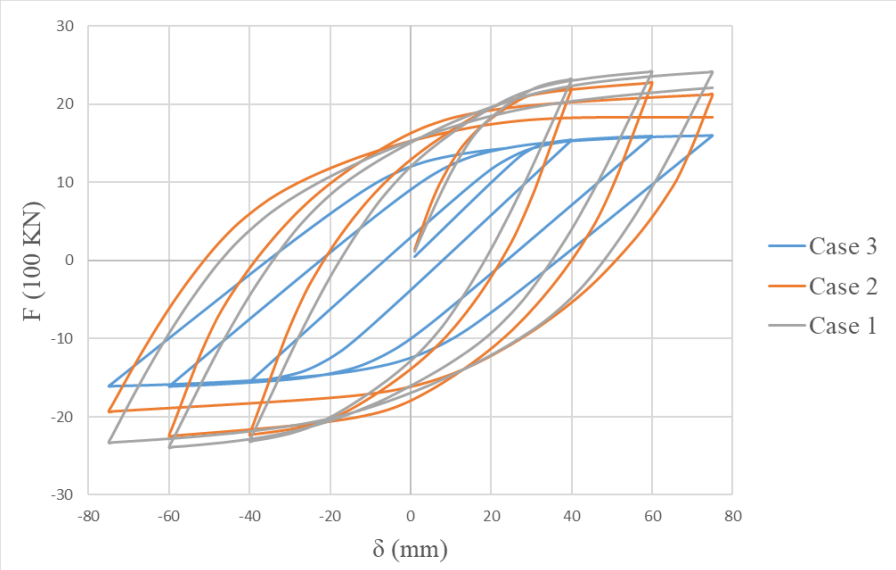

Fig. 5.3. Hysteresis loops resulted for frame modelled as per Cases 1, 2 and 3 including fatigue subjected to quasi-static cyclic loading using cyclic-pushover analysis

The effect of fatigue in material stage is calculated in each integration point defined in the element and the total change in stiffness and hardening is shown in the frame scale. As an example, the stress strain diagram in different directions and damage evolution due to fatigue effect on the right side of the right element on top flange in the first beam cross-section in the model adjusted to Case 3 is presented below in Figs. 5.4 to 5.7. In the Table 5.1, the reduction in effective stress slope due to damage evolution is also presented.

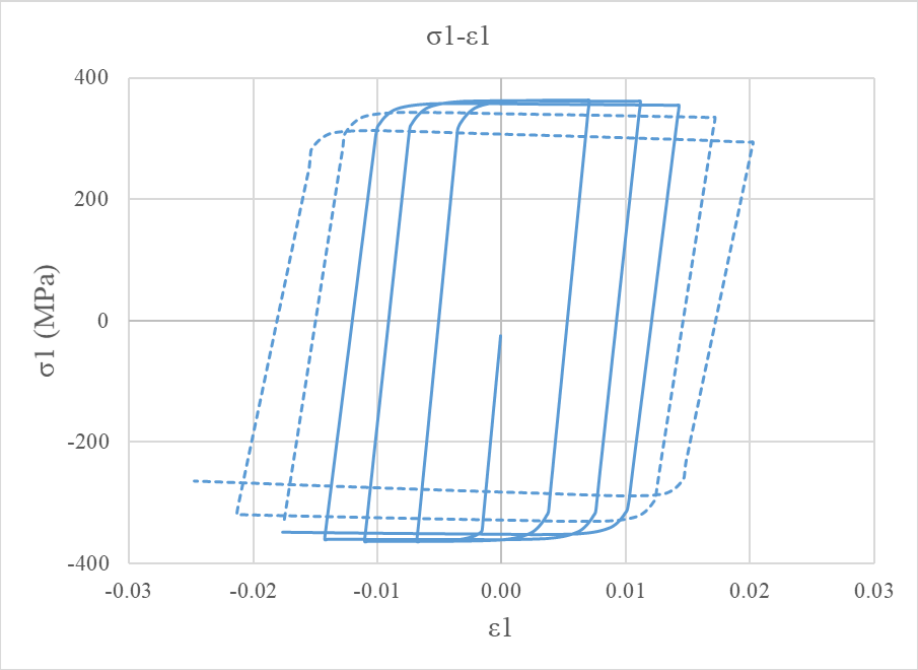

Fig. 5.4 Stress-strain diagram in direction 1

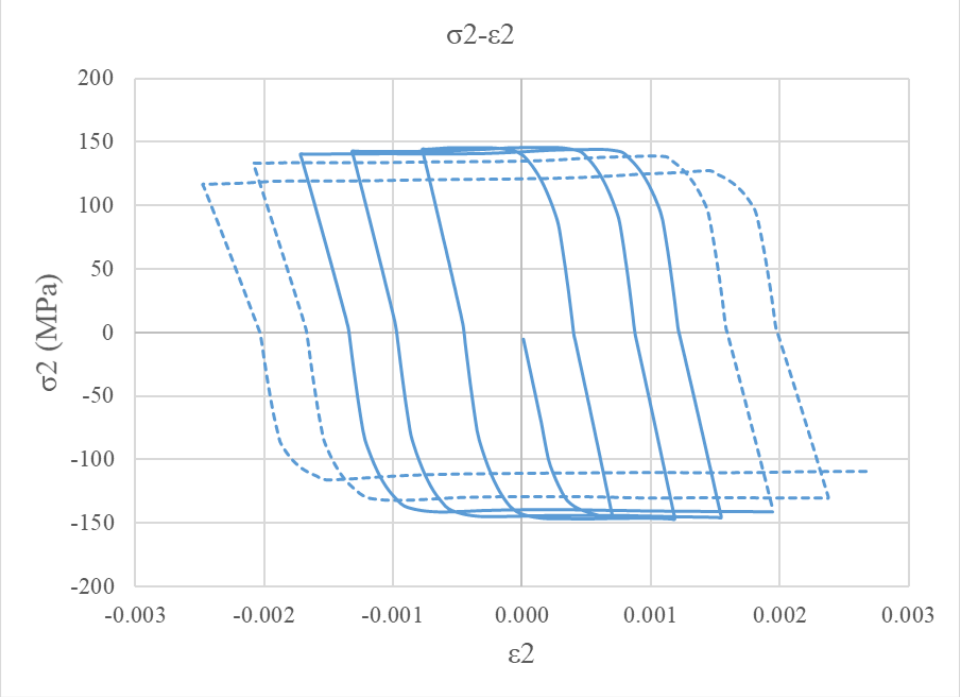

Fig. 5.5 Stress-strain diagram in direction 2

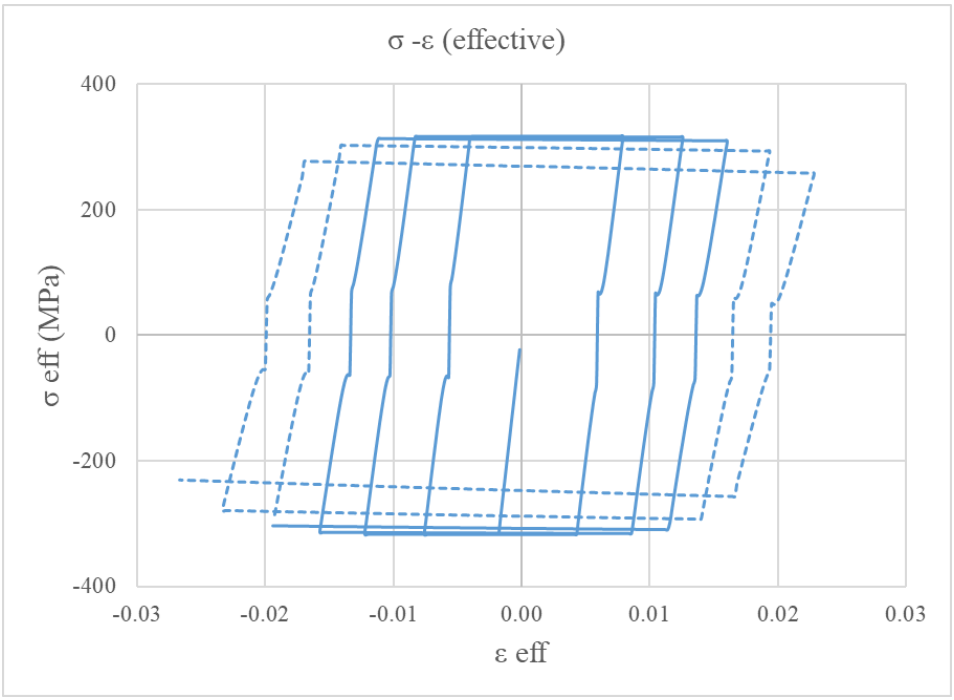

Fig. 5.6 Effective stress-strain diagram

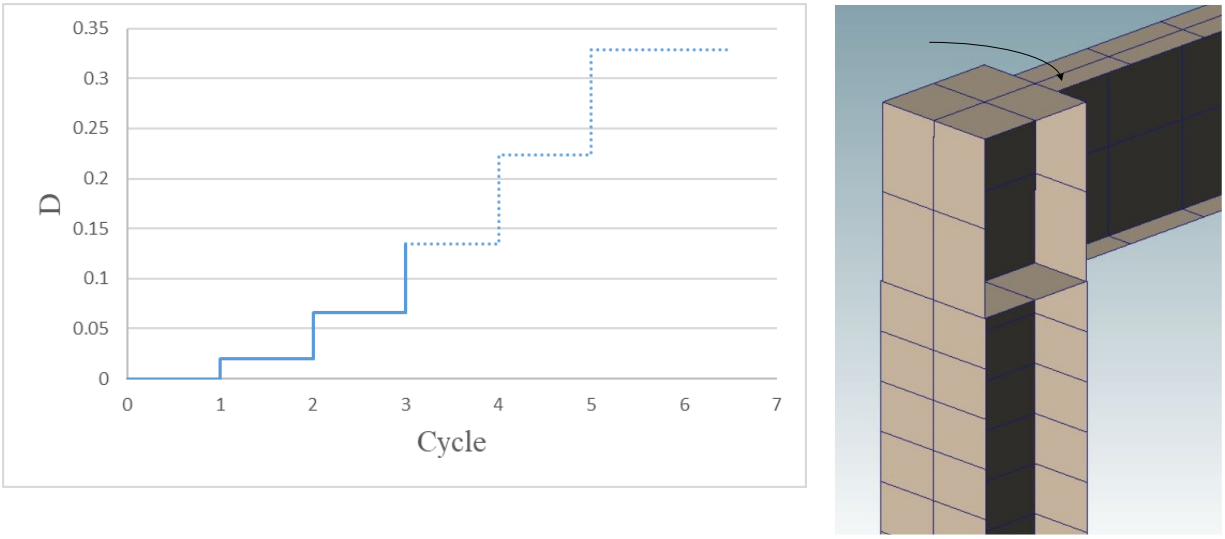

Fig.5.7 Damage variable evolution in different cycles

Table 5.1 Damage evolution comparison

Cycle	E model (MPa) using σ-ε slope	Damage	E (MPa) using formula
0	179055.947		
1	169244.919	0.019639	172091.944
2	152905.100	0.066377	156074.530
3	132832.214	0.135142	133930.249
4	108046.650	0.223154	108058.430
5	81677.573	0.328411	80759.902
6	55414.956	0.448521	54456.045

5.2.3 Comparative response of frame response modelled with and without fatigue according to Case 1 under cyclic pushover analysis

Considering the same quasi-static cyclic loading presented in Fig. 5.2a, the Case 1 model with and without fatigue is employed and the hysteresis loops under cyclic pushover analysis is presented in Fig. 5.8. It is shown in the graph that fatigue is affecting the structural response in Case 1 (beam theory) and the effect is shown as both stiffness degradation and yield surface.

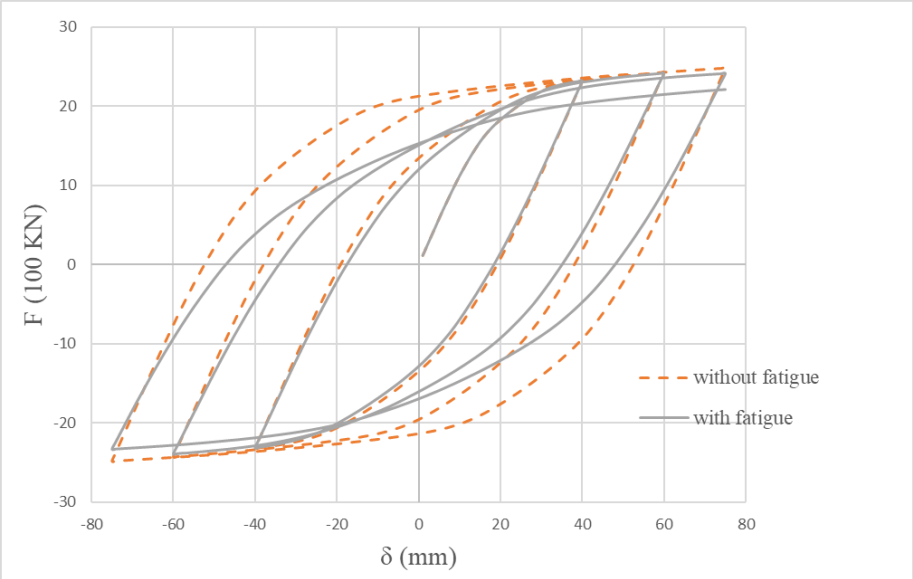

Fig. 5.8 Hysteresis loops resulted for frame modelled as per Case 1 with and without fatigue subjected to quasi-static cyclic loading using cyclic-pushover analysis

It is shown in the graph that fatigue is affecting the structural response in Case 1 (beam theory) and the effect is shown as both stiffness degradation and yield surface.

5.2.4 Comparative response of frame response modelled with and without fatigue according to Case 2 under cyclic pushover analysis

Considering the same quasi-static cyclic loading presented in Fig. 5.2a, the Case 2 model with and without fatigue is employed and the hysteresis loops under cyclic pushover analysis is presented in Fig. 5.9. The effect of fatigue in the Case 2 is more considerable since with the same parameters assumed for fatigue in all cases in the yield surface. The ratcheting behavior is shown in the Fig.5.9.

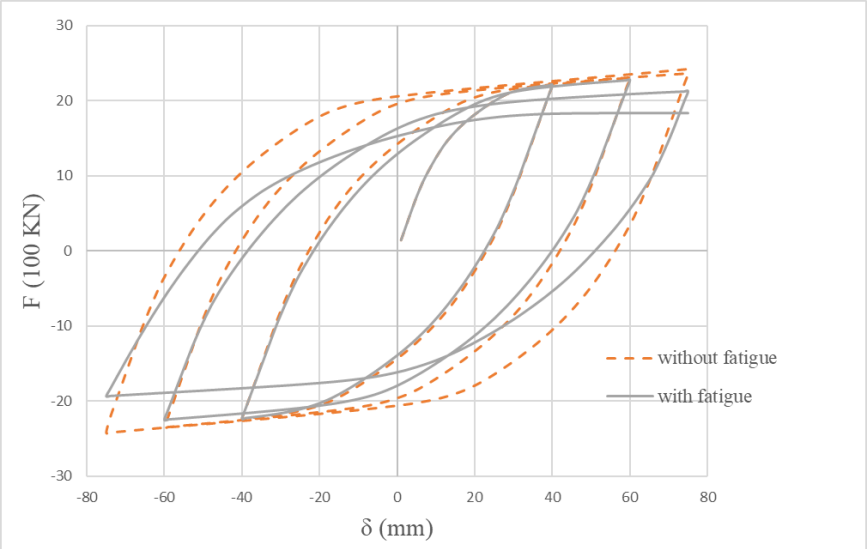

Fig. 5.9 Hysteresis loops resulted for frame modelled as per Case 2 with and without fatigue subjected to quasi-static cyclic loading using cyclic-pushover analysis

5.2.5 Comparative response of frame response modelled with and without fatigue according to Case 3 under cyclic pushover analysis

Considering the same quasi-static cyclic loading presented in Fig. 5.2a, the Case 3 model with and without fatigue is employed and the hysteresis loops under cyclic pushover analysis is presented in Fig. 5.10. The Case 3 seems to be affected by fatigue mostly in stiffness degradation. In the third cycle an effect of ratcheting is shown about deflection around -75 (mm).

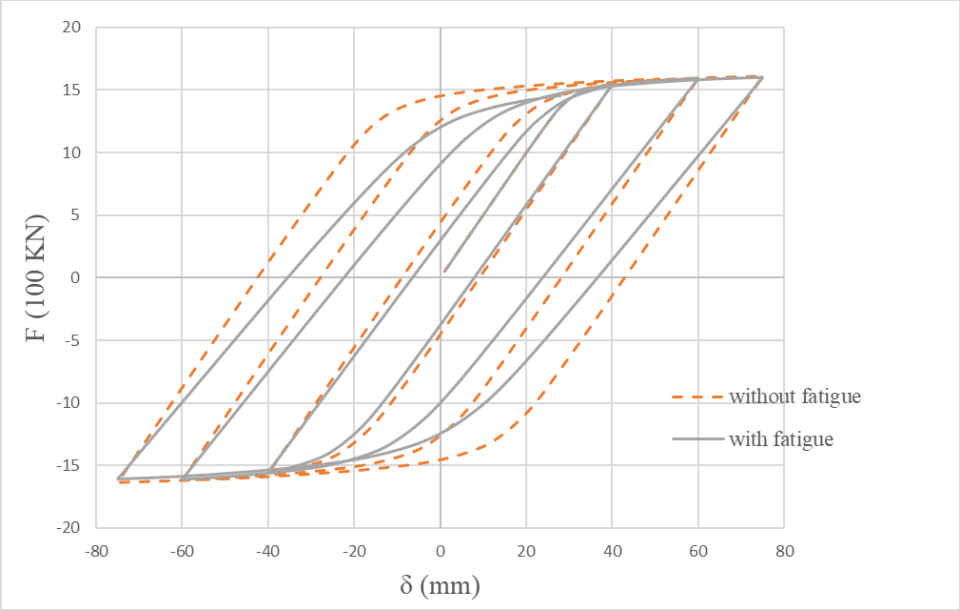

Fig. 5.10 Hysteresis loops resulted for frame modelled as per Case 3 with and without fatigue subjected to quasi-static cyclic loading using cyclic-pushover analysis

5.2.6 Local modes captured using modal analysis of Case 3

Performing modal analysis, different probable deformations shapes can also be captured. In this section, different mode shapes and related eigenvalues are presented.

In Tab.5.2 are presented the local mode shapes affecting the beam member. The deformed shape associated to each local mode is depicted in Figs. 5.11 – 5.21.

Table 5.2 Eigenvalues for different local mode shape for the Case 3

Mode	1	2	3	4	5	6
Eigenvalue	0.0211	0.0426	0.0671	0.0754	0.0759	0.0874
Mode	7	8	9	10	11	12
Eigenvalue	0.0882	0.0907	0.1051	0.1066	0.1243	0.1337

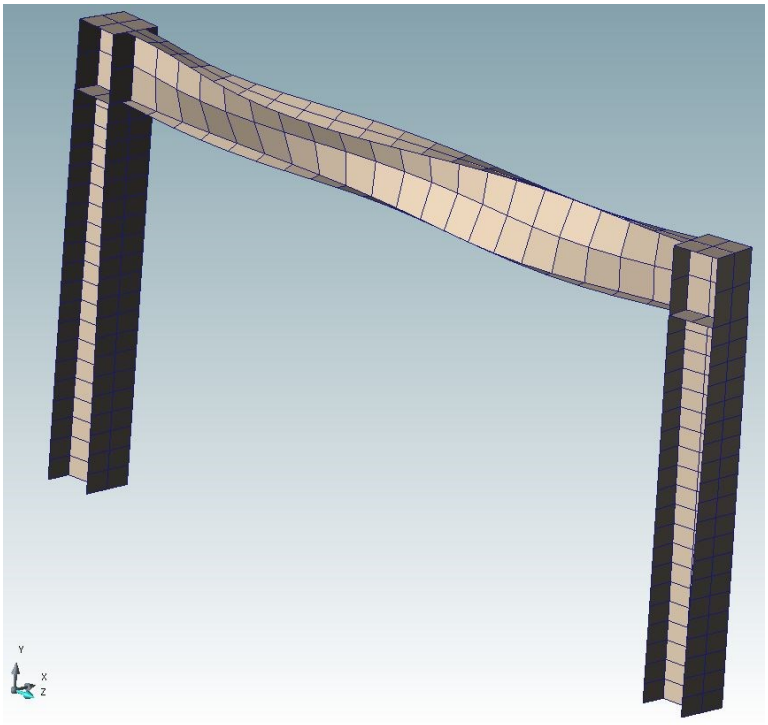

Fig.5.11 The second mode shape for capturing local buckling

The torsional deformation is more noticeable in the second and third mode shapes.

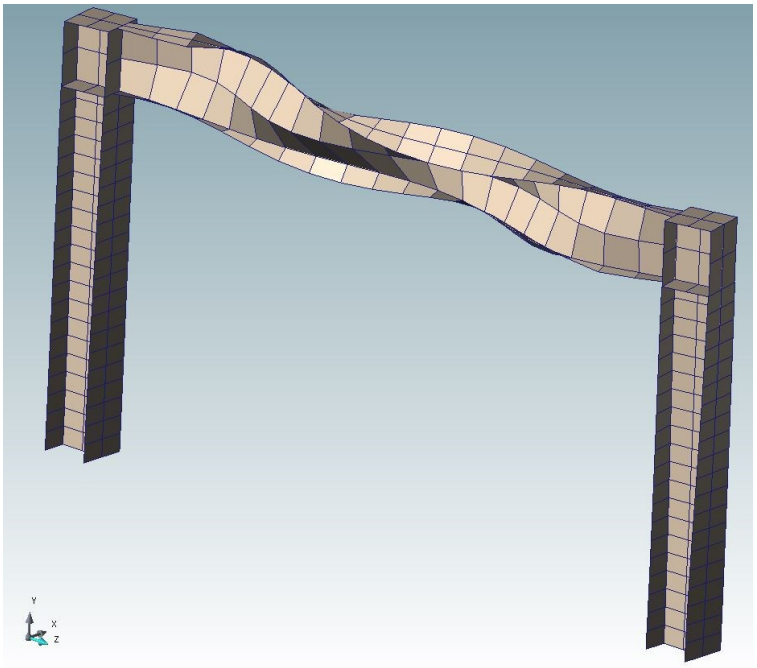

Fig.5.12 The third mode shape for capturing local buckling

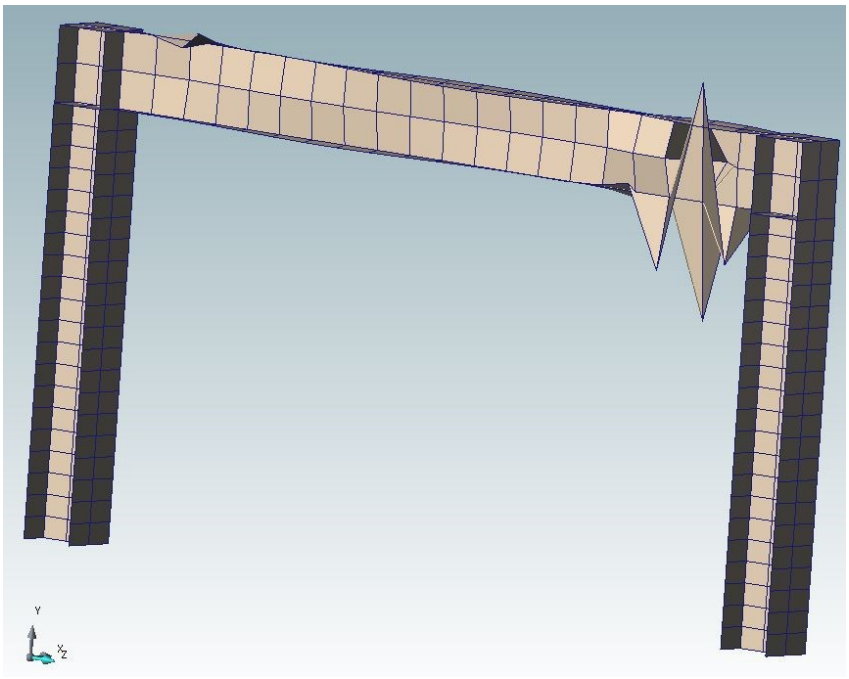

Fig.5.13 The fourth mode shape for capturing local buckling

In the fourth and fifth modes, the deformation is more local, as shown in Fig.5.13 and Fig.5.14.

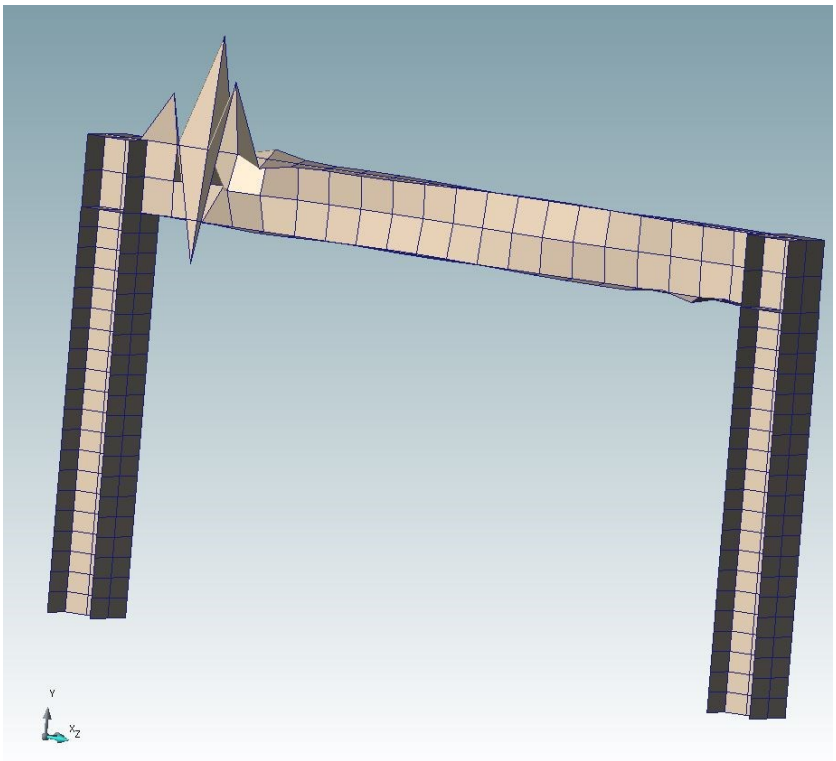

Fig.5.14 The fifth mode shape for capturing local buckling

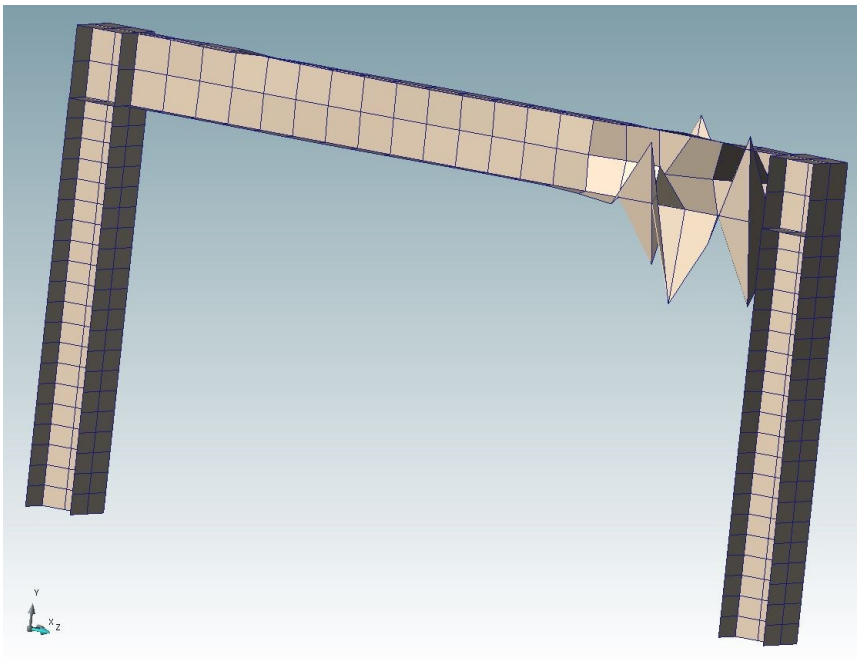

Fig.5.15 The sixth mode shape for capturing local buckling

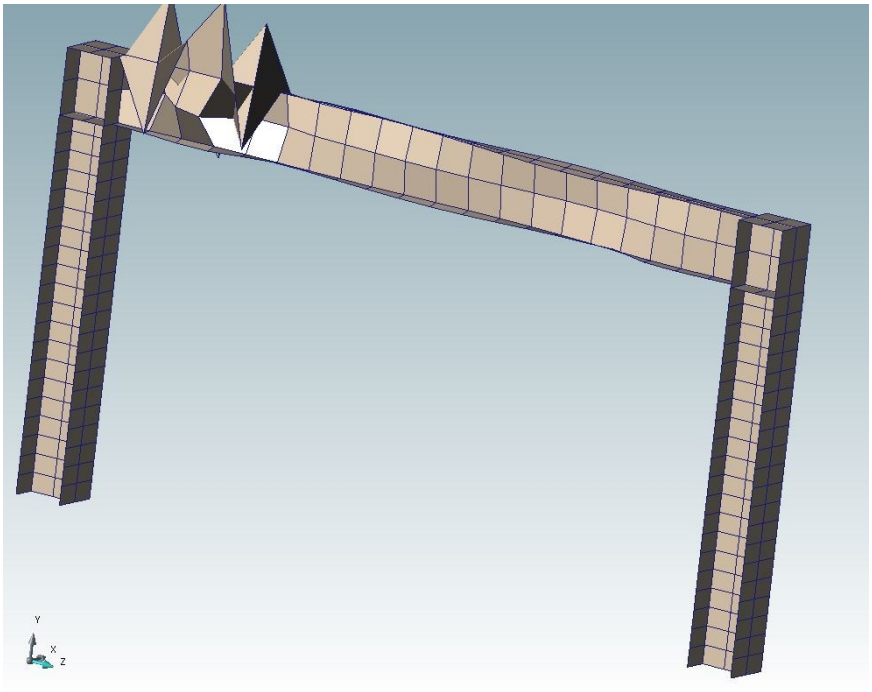

Fig.5.16 The seventh mode shape for capturing local buckling

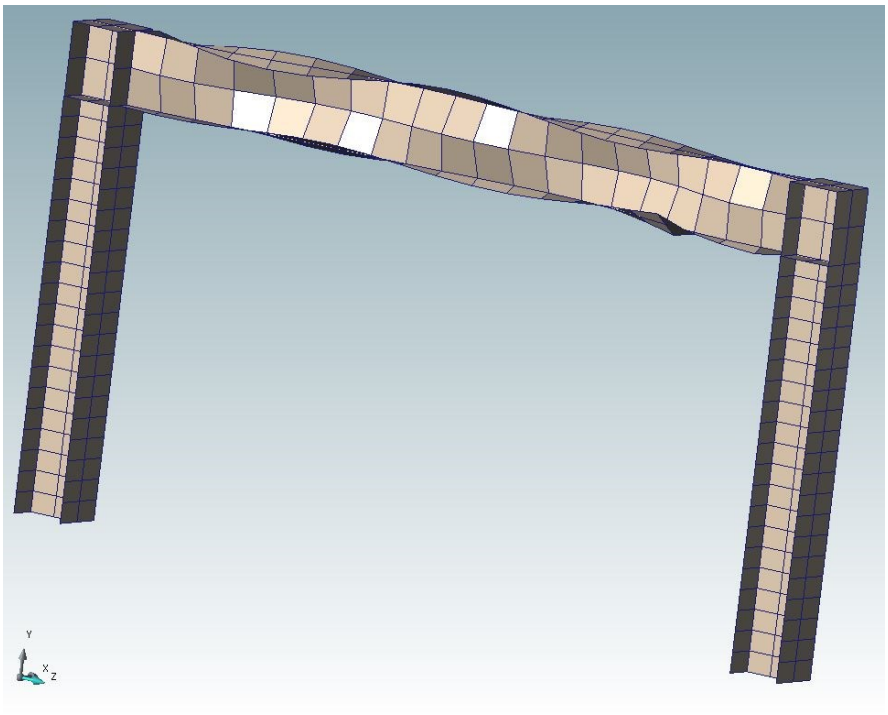

Fig.5.17 The eighth mode shape for capturing local buckling

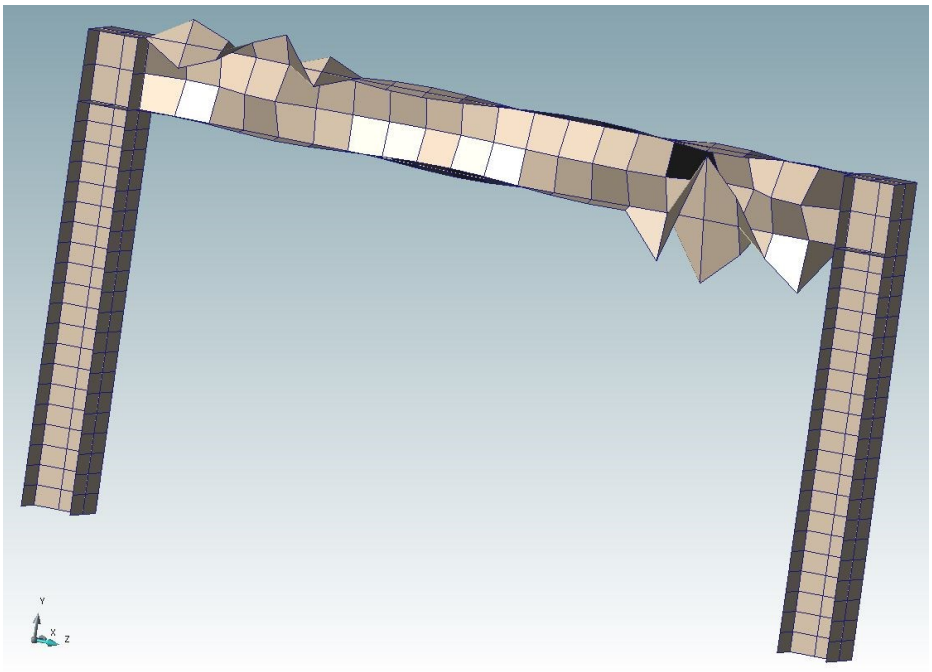

Fig.5.18 The ninth mode shape for capturing local buckling

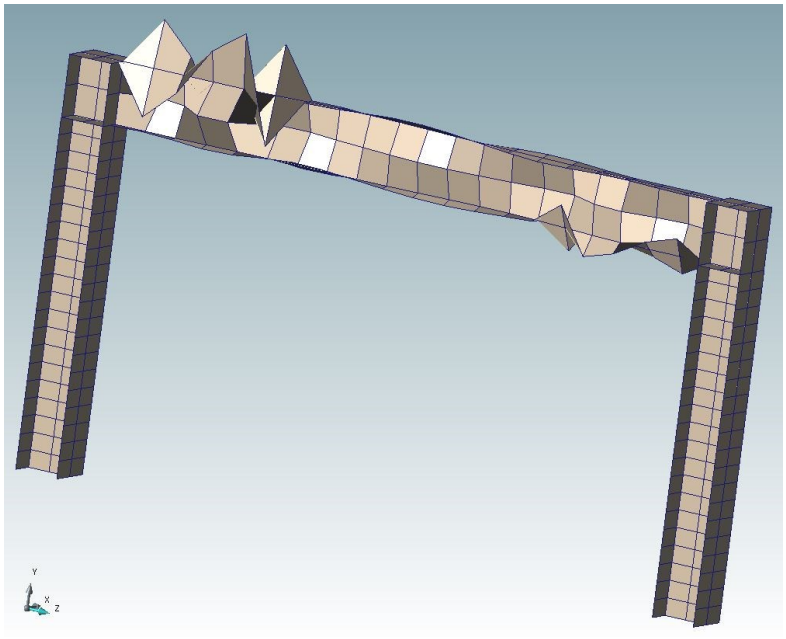

Fig.5.19 The tenth mode shape for capturing local buckling

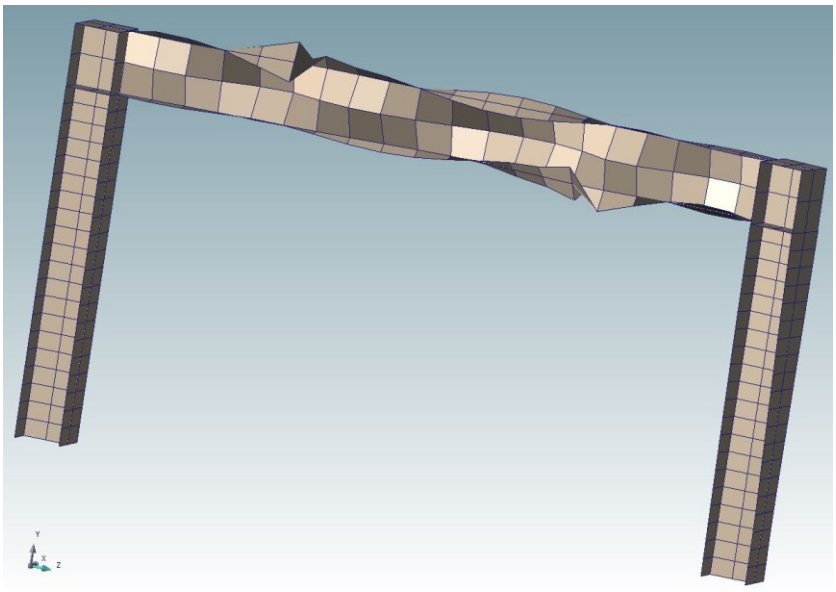

Fig.5.20 The eleventh mode shape for capturing local buckling

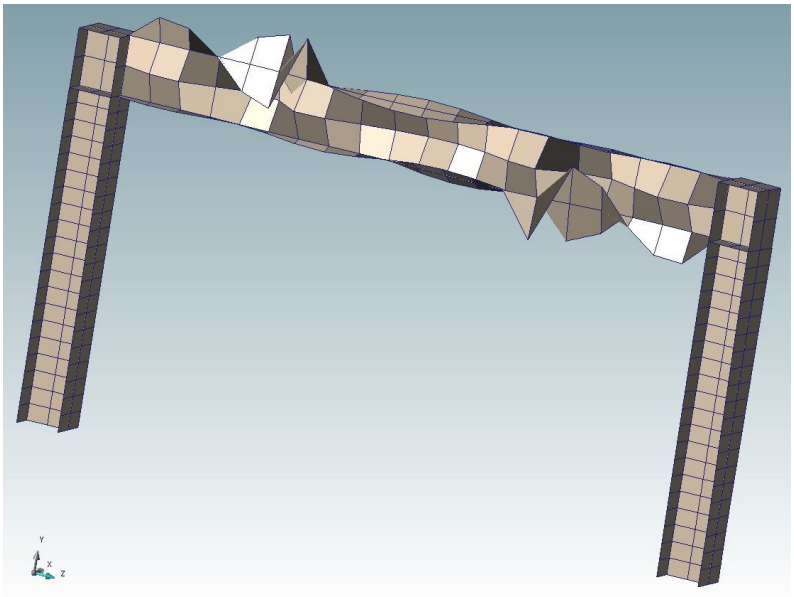

Fig.5.21 The twelfth mode shape for capturing local buckling

As presented in Table 5.1, the mode shapes after third mode have less effect. The more considerable mode shapes are the first, second, and third modes. This is also another capability of the element presented to capture local mode shapes.

5.2.7 Effect of initial imperfection on the nonlinear analysis results

In Fig.5.22 the comparison between the mode shapes introduced as the initial imperfection is presented. As mentioned before, in the previous models, the first buckling mode shape was introduced as the initial imperfection in the model. It is worth to mention that introducing different mode shapes also can affect the overall behavior of the structure.

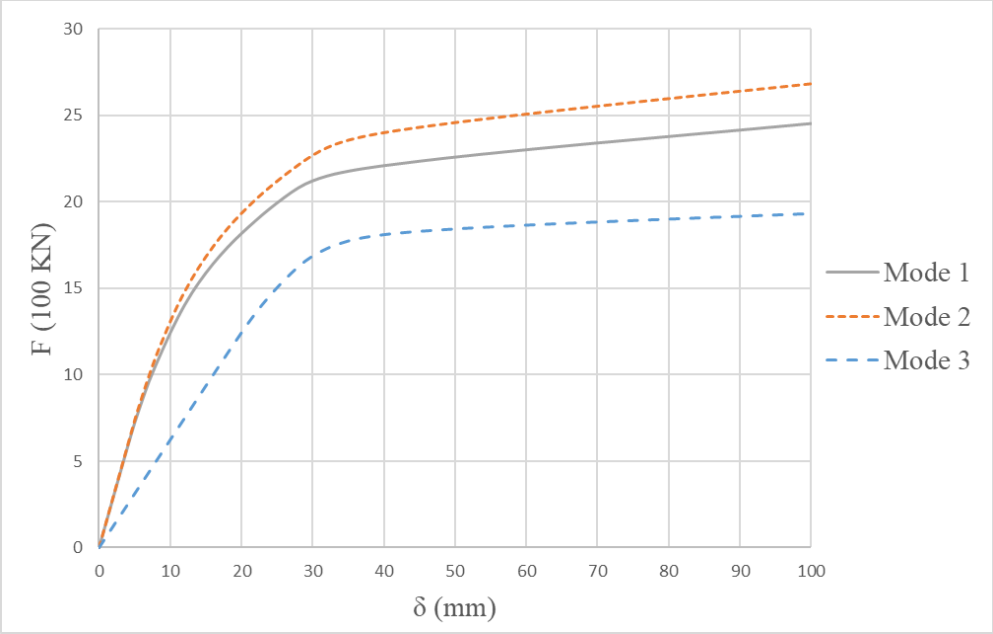

Fig.5.22 Pushover analysis results using different initial imperfections in Case 2.

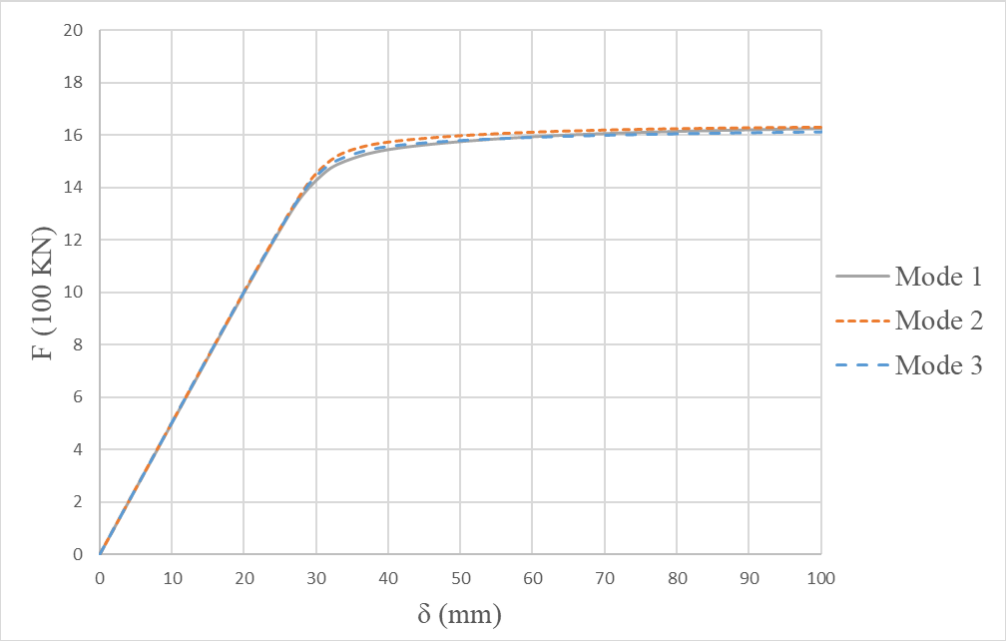

Fig.5.23 Pushover analysis result using different initial imperfections in Case 3.

CHAPTER 6: CONCLUSIONS AND FUTURE WORK

6.1 Conclusions

This study was conducted to investigate the low-cycle fatigue effect in material properties on the structural behavior under the Continuum Damage Plasticity framework using cumulative plastic work. The effect of the cyclic load was considered as stiffness degradation in elastic modulus and change in hardening parameter in the material level. The shell-type element is used to model the thin-walled section. The presented shell-type element is composed of a membrane-type element with a drilling degree of freedom and a plate-type element, called Discrete Kirchhoff Quadrilateral. Therefore, the shell-type element used in this study has six-degrees of freedom on each node resulting in 24-degrees of freedom for each element. In the study, second-order geometric nonlinearity, as well as, material nonlinearity analysis, was performed. Linear Elastic Buckling analysis was also performed to introduce imperfections using the buckling modes of the modelled structure. The Multi-point Constraint method is also used to simulate the behaviour of beam-type model.

As a verification, a 60-element I-shaped section model assigned to a cantilever beam is used for nonlinear analysis, and a mesh sensitivity analysis was also performed using a 480-element model. A quasi-static cyclic load-displacement pushover analysis is performed using the presented load protocol.

As a case study, a one-bay single-story frame structure is modelled using the I-shaped cross-section element. For modelling, the aforementioned shell-type element is used. In the modelling, thicker elements are used inside the panel zone to have rigid movement and deformations in the zone. Three different types of modelling the frame are presented in the study. The response of the structure is presented as a result of a quasi-static cyclic load-displacement pushover analysis using

the presented load protocol. The first buckling mode shape is introduced as imperfection in the model considering the boundary condition related to each case.

Findings and observations gathered as a result of this study are as follows:

- The developed program is capable of performing quasi-static cyclic pushover analysis on the frame structure with and without considering the fatigue effect. It is shown that low cycle fatigue effect can change the response of the structure. Figs 5.8 to 5.10 show that even after a few cycles, global stiffness as well as, the peak load carrying capacity starts getting effected.
- Figs 5.1 show that when local deformations are considered in the push over analysis, the global stiffness as well as the peak load carrying capacity are significantly affected. Therefore, shell type analysis that is capable of capturing nonlinear geometric, as well as, material behaviour might be necessary for an accurate capacity analysis of steel frames.
- Initial imperfection might influence the nonlinear analysis results significantly (Fig 5.22).
- For nonlinear analysis, identifying the triggering mechanisms to obtain results beyond stability limits are essential to avoid convergence problems. After several different approaches we could avoid convergence related problems by adopting buckling modes as the initial imperfection in the system.
- Agreement with known cases and mesh sensitivity analyses show that the shell element formulation based on the DKQ plate and Drilling Membrane adopted in this study is very efficient in producing accurate results with minimal number of elements.
- As one of the main objectives of the study is to gain access to details in material and structural modelling, the tool developed in Fortran language for this study has been sufficiently validated by comparisons with other solutions in literature. As such, many

practical components make the tool useful to run parametric studies with minimal modelling effort, such as automatic mesh generation, introduction of number of mode shapes as imperfections, direct access to elastic, plastic and damage related parameters. This accessibility to material and structural model details also provides unique opportunity to pursue future research work.

6.2. Future work

Future research work can be conducted in the following topics:

- Anisotropic damage as a result of fatigue effect can also be modelled using the Continuum Damage Plasticity framework. Some material can behave differently in different directions due to fatigue damage accumulation.
- A dynamic analysis module can be introduced in order to run a time-history analysis under earthquake loads. Different ground motions can also have cyclic effects on the frame structure that the fatigue effect is needed to be taken into account.
- Steel-plate shear walls can be modelled using the shell-type element. Local deformations can be modelled using shell elements.
- A multi-scale analysis framework can be introduced in order to avoid using shell elements for the whole structure. Using a multi-scale analysis framework, only critical parts of the frame that goes through local buckling can be modelled with shell elements, and the rest of the structure can be modelled by using beam elements. This may result in an economic modelling approach and can be made applicable to high-rise steel frame structures.

References:

Aboutalebi, F.H., Poursina, M., Nejatbakhsh, H., Khataei, M. (2018). "Numerical simulation and experimental validation of a proposed ductile damage model for DIN1623 St12 steel" *Journal of Engineering Fracture Mechanics*, 192:276-289.

Ahmad, S., Irons, B.M., Zienkiewicz, O.C. (1970). "Analysis of thick and thin shell structures by curved finite elements". *International Journal for Numerical Methods in Engineering*, 2:419-451.

Amiable, S., Chapuliot, S., Constantinescu, A., Fissolo, A. (2006). "A comparison of lifetime prediction methods for a thermal fatigue experiment". *International Journal of Fatigue.* 28(7):692–706. http://doi.org/10.1016/j.ijfatigue.2005.09.002

Areias, P.M.A., Song, J.H., Belytschko, T. (2005). "A finite-strain quadrilateral shell element based on discrete Kirchhoff-Love constraints" *International Journal for Numerical methods in Engineering*. 64:1166-1206.

Armero, F., Oller, S. (2000). "A general framework for continuum damage models. I. Infiniterimal plastic damage models in stress space." *International Journal of Solids and Structures*. 37, 7409-7436.

Armero, F., Linder, C., (2009). "Numerical simulation of dynamic fracture using finite elements with embedded discontinuities". *International Journal of Fracture*. 160:119-141.

Ayhan, B., Jehel, P., Bramcherie, D., Ibrahimbegovic, A. (2013) Coupled damage-plasticity model for cyclic loading: Theorical formulation and numerical implementation. *Journal of Engineering Structures*. 50, 30-42

Batoz, J.L., Tahar M.B. (1982). “Evaluation of a new quadrilateral thin plate-bending element”. *International Journal of Numerical Methods in Engineering* 18:1655–1677

Bosco, M., Tirca, L. (2017) “Numerical simulation of steel I-shaped beams using a fiber-based damage accumulation model”. *Journal of Constructional Steel Research*. 133:241–255

Braithwaite, F. (1854). “On the Fatigue and Consequent Fracture of Metals”, *Minutes of Proc. ICE* 463.

Brünig, M., Gerke, S. (2011). “Simulation of damage evolution in ductile metals undergoing dynamic loading conditions”. *International Journal of Plasticity*. 27:1598-1617.

Chen, W.F., Han, D.J. (1988). “Plasticity for structural engineers” *Springer-Verlag*.

Cook, R.D. (1994). “Four-node plat shell element: drilling degrees of freedom, membrane-bending coupling, warped geometry and behaviour”. *Journal of Computers and Structures*. 50(4):549-555.

Chapelle, D., Bathe, K.J. (1998). “Fundamental considerations for the finite element anlysis of shell structures” *Journal of computers and structures*. 66(1):19-36.

Cheung, Y.K., Zinkiewicz, O.C. (1965). “Plates and tanks on elastic foundation – an application of finite element method”. *International Journal of Solids and Structures*. 1(4):451-461.

Engelhardt, M.D., Sabol T.A., (1994). “Testing of welded steel moment connections in response to the Northridge Earthquake”, *Progress Report to the AISC Advisory Subcommittee on Special Moment Resisting Frame Research*

Ellyin, F, Kujawski, D. (1984). “Plastic strain energy in fatigue failure”, *Journal of pressure vessel technology,* 106:342-347.

Erkmen, R.E. (2013). “Bridging multi-scale approach to consider the effects of local deformations in the analysis of thin-walled members”. *Computational Mechanics*. 52:65-79.

Erkmen, R.E (2019) “Advanced Finite Element Methods in Structural Mechanics: Lecture notes” Concordia University.

Ewing, J.A. Humfrey, J.C.W. (1903). “The Fracture of Metals under Repeated Alternations of Stress”. Philosophical Transactions, *Royal Society London*, CC 241.

Fafard, M., Beauliu, D., Dhatt, G. (1987). “Buckling of thin-walled members by finite elements”. *Computers & Structures*. 25(2):183-190.

Farahmand, B., Bokhrath, G., Glassco, J. (1997). “Conventional Fatigue (High- and Low-Cycle Fatigue). In: Fatigue and Fracture Mechanics of High-Risk Parts”. *Springer, Boston, MA*. https://doi.org/10.1007/978-1-4615-6009-8_2

Gruttmann, F., Wagner, W., Wriggers, P. (1992). “A nonlinear quadrilateral shell element with drilling degree of freedom”. *Archive of Applied Mechanics*. 62:474-486.

Hughes, T.J.R., Liu, W.K. (1981). “Nonlinear finite element analysis of shells: Part1: Three-dimensional shells”. *Journal of Computer Methods in Applied Mechanics and Engineering*. 26:331-362.

Hutchinson, J.W., Thompson, J.M. (2018). “Imperfections and energy barriers in shell buckling” *International Journal of Solids and Structures*. 148-149:157-168.

Ibrahimbegovic, A. (1994a). “Stress resultant geometrically nonlinear shell theory with drilling rotations-Part1: A consistent formulation” *Journal of Computer methods in applied mechanics and Engineering*. 118:265-284

Ibrahimbegovic, A. (1994b). “Stress resultant geometrically nonlinear shell theory with drilling rotations-Part2: Computational aspects” *Journal of Computer methods in applied mechanics and Engineering.* 118:285-308

Ibrahimbegovic, A, Taylor RL, Wilson EL (1990). “A robust quadrilateral membrane finite element with drilling degrees of freedom”. *International Journal of Numerical Methods in Engineering* 30:445–457

Ibrahimbegovic, A., Jehel, P., Devanne, L. (2008). “Coupled damage-plasticity constitutive model and direct stress interpolation”. *Journal of Computational Mechanics* 42,1-11

Inglessis, P. (1999) Model of damage for steel frame members. *Journal of Engineering Structures* 21, 954-964.

Jetteur, P., Frey, F. (1993). "A four node Marguerre element for nonlinear shell analysis", *Engineering Computations* 3(4):276 - 282

Krajcinovic, D. (1996). “Damage mechanics”. *North-Holland Series*

Krupp, U. (2007). “Fatigue crack propagation in metals and alloys: Mictrostructural aspects and modelling” *Wiley-VCH Verlag GmbH and Co.*

Lemaitre, J. (1994). “Mechanics of Solid Materials” *New York: Cambridge University Press*. 1-10.

Lemaitre, J. (1992). “A course on damage mechanics”, *Springer, Berlin; 2nd Edition* (1996) https://doi.org/10.1007/978-3-642-18255-6

Lua J., Zhang T., Fang E., Song J. (2016). "Explicit phantom paired shell element approach for crack branching and impact damage prediction of aluminum structures". *International Journal of Impact Engineering,* 87:28-43.

Luo, Y., Zhan, J., Liu, P., (2019). "Buckling assessment of thin-walled plates with uncertain geometrical imperfections based on non-probabilistic field model" *Journal of thin-walled structures*. A45:106435.

Martinez, X., Oller, S., Barbu, L.G., Barbat, A.H., du Jesus, A.M.P. (2015). "Analysis of ultra-low cycle fatigue problems with the Barcelona plastic damage model and a new isotropic hardening law". *International Journal of Fatigue.* 73:132-142.

McClintock, F. A. (1968). "A criterion for ductile fracture by the growth of holes". *Journal of Applied Mechanics* 35,363-371.

Miner, M.A. (1954). "Cumulative Damage in Fatigue". *Transactions ASME – Journal of Applied Mechanics*, 12 A159

Murakami, S. (2012). "Continuum damage mechanics: A continuum mechanics approach to the analysis of damage and fracture", Springer. https://doi.org/10.1007/978-94-007-2666-6

Murakamai, Y., Ferdous, M.S., Makabe, C., (2016). "Low-cycle fatigue damage and critical crack length affecting loss of fracture ductility", *International Journal of Fatigue*. 82:89-97

Neuber, H. (1961). "Theory of Stress Concentration for Shear-Strained Prismatic Bodies with Arbitrary Nonlinear Stress Strain Law", *Journal of Applied Mechanics*, 28:544.

Nguyen-Van, H., Mai-Duy, N., Tran-Cong, T. (2009). "An improved quadrilateral flat element with drilling degrees of freedom for shell structural analysis" *Journal of Tech Science Press*.

Oden, J., Sato, T. (1967). “Finite strain and displacements of elastic membranes by the finite element method”. *International journal of Solids and Structures*. 3(4):471-488.

Palmgreen, A. (1924). “Die Lebensdauer von Kugellagern”, *VDI-Zeitschrift*, 68 339.

Papadopoulos, V., Soimiris, G., Papadrakakis, M., (2013). “Buckling analysis of I-section portal frames with stochastic imperfections”. *Engineering Structures*. 47:54-66.

Paul, S.K. (2014). “A multi-axial low cycle fatigue life prediction model for both proportional and non-proportional loading conditions”. *Journal of Material Engineering and Performance.* 23(9):3100-3107.

Radu, D., Sedmak, A., Sedmak, S., Li, W. (2020). “Engineering critical assessment of steel shell structure elements welded joints under high cycle fatigue”. *Journal of Engineering Failure Analysis.* 114:104578.

Rashid, Y.R. (1966). “Analysis of axisymmetric composite structures by the finite element method” *Journal of Nuclear Engineering and Design*. 3(1):163-182.

Riberio, J., Santiago, S., Riguerio, C. (2016). “Damage model calibration and application for S355 steel”. *21st European Conference on Fracture, ECF21*, June, Catania, Italy.

Roth, C.C, Mohr, D. (2014). “Effect of strain rate on ductile fracture initiation in advances high strength steel sheets: Experiment and modelling”. *International Journal of plasticity*. 56:19-44.

Shayan, S. Rasmussen, K. Zhang, H. (2014). “On the modelling of initial geometric imperfections of steel frames in advanced analysis”. *Journal of Construction Steel Research*. 98:167-177.

Smith, R.A. (1990). “The Versailles Railway Accident of 1842 and the First Research into Metal Fatigue”, *Proc. Fatigue* ’90 – 2033.

Springer, M., Pettermann, H.E. (2018). "Fatigue life predictions of metal structures based on low-cycle, multi-axial fatigue damage model". *International Journal of Fatigue.* 116:355-365. https://doi.org/10.1016/j.ijfatigue.2018.06.031

Swift, H.Q. (1952). "Plastic instability under plane stress*". Journal of the mechanics and physics in solids*. 1:1-18.

Teng. J.G. Hong. T. (1998). "Nonlinear thin shell theories for numerical buckling prediction" *Journal of thin-walled structures*. 31:89-115.

Tong. P., Pian T.H.H. (1967). "The convergence of finite element method in solving elastic problems". *International Journal of Solids and Structures*. 3(5):865-879.

de Veubeke, B.F. (1968). "A confirming finite element for plates". *International Journal of Solids and Structures.* 4(1):95-108.

Vose, E. (1948). "The relationship between stress and strain of homogenous deformations". *Journal of institute of metals*. 74:537-562.

Wackerfub, J. (2008). "Efficient finite element formulation for the analysis of localized failure in beam structures". *International Journal for Numerical methods in Engineering*. 73:1217-1250.

Wang, F.Y., Xu, Y.L., Sun, B., Zhu, Q. (2019). "Dynamic stress analysis for fatigue damage prognosis of long-span bridges". *Journal of Structure and Infrastructure Engineering*. 15(5):582-599.

Wempner, G. (1969). "Finite element, finite rotations and small strains of flexible shells". *International Journal of Solids and Structures.* 5(2):117-153.

Wöhler, A. (1870). “Über die Festigkeits-Versuchemit Eisen und Stahl” *Zeitschrift für Bauwesen*, 20:73

Xue, J., Shang, D.G., Li, D.H., Li, L.J., Xia, Y., Hui, J. (2019). “Online multi-axial fatigue damage evaluation method by real-time cycle counting and energy-based critical plane criterion”. *Journal of Fatigue and Fracture of Engineering Materials and Structures*. 43:1184-1198.

Zhan, Z., Hu, W., Meng, Q., Shi, S. (2016). “Continuum damage mechanics-based approach to fatigue life prediction for 7050-T7451 aluminum alloy with impact pit”. *International Journal of Damage Mechanics*. 25(7):943-966.